



# Thermal properties of spark plasma sintered Inconel 625 modified by titanium zirconium mixed carbide

Paweł Rutkowski<sup>1</sup> · Jan Huebner<sup>1</sup> · Adrian Graboś<sup>2</sup> · D. Kata<sup>1</sup> · Katarzyna Pasiut<sup>1</sup> · Bartosz Handke<sup>3</sup> · Paweł Nieroda<sup>4</sup>

Received: 10 November 2022 / Accepted: 6 May 2023 / Published online: 30 May 2023  
© The Author(s) 2023

## Abstract

Nickel-based superalloys are an important group of advanced engineering materials used for high-temperature and/or corrosive environments. Lately, in order to improve their mechanical properties, carbide reinforcement is added to a metal matrix, creating composites of improved hardness, shear resistance, or tensile resistance. In order to preserve the wide applicability of those materials, thermal properties, and corrosion resistance must also be evaluated. Presented research evaluated the thermal properties of Inconel 625—(Ti,Zr)C<sub>0.85</sub> composites obtained at 1000 °C by spark plasma sintering process. Sinters containing 5–20 mass% of carbide phases were initially characterized in terms of their density, phase composition, and microstructure. A thorough examination of their thermal properties included: dilatometry, laser flash analysis, and differential scanning calorimetry. Conducted experiments revealed that a growing amount of carbide reinforcement decreased the thermal diffusivity and conductivity of samples. Other materials had a nonlinear correlation with that parameter. Performed analysis allowed to make an initial evaluation of oxidation resistance at 800 °C. It was shown that above 5 mass% addition of (Ti,Zr)C<sub>0.85</sub> there is a considerable mass gain change shown by samples during the first hour of oxidation before passive layers were created. Suitable chemical reactions were predicted in order to describe the oxidation process of obtained composites.

**Keywords** Inconel 625 · Titanium-zirconium carbide · SPS · Microstructure · Corrosion resistance · Thermomechanical properties

## Introduction

Ni-based superalloys have wide applications, such as shipboard, aerospace, and automotive components [1–4]. They are typically used in chemically aggressive high-temperature environments [5–7], where they stand out in terms of tensile strength properties and creep resistance [4, 8, 9]. To achieve progress in mentioned technologies, hardness, wear, and creep resistance together with thermal stability at elevated temperatures are to be improved. In order to do that, metal matrix composites utilizing them as base material were introduced. High hardness and good and in many cases excellent wettability of many carbides, makes them a considerable choice for such systems [10–13].

In order to improve the mechanical properties of Inconel 625 the ceramic phases such as carbides and diborides of transition metals are used. In the case of carbides, NbC, WC, SiC, and TiC were so far used to a considerable degree of success [14–17], while in the case of borides, it was solely TiB<sub>2</sub> [18]. However, except for better mechanical properties,

✉ Paweł Rutkowski  
pawelr@agh.edu.pl; pawel.rutkowski@agh.edu.pl

<sup>1</sup> Faculty of Materials Science and Ceramics, Department of Ceramics and Refractories, AGH University of Science and Technology, A. Mickiewicza Av. 30, 30-059 Krakow, Poland

<sup>2</sup> Academic Centre for Materials and Nanotechnology, AGH University of Science and Technology, A. Mickiewicza Av. 30, 30-059 Krakow, Poland

<sup>3</sup> Faculty of Materials Science and Ceramics, Department of Silicate Chemistry and Macromolecular Compounds, AGH University of Science and Technology, A. Mickiewicza Av. 30, 30-059 Krakow, Poland

<sup>4</sup> Faculty of Materials Science and Ceramics, Department of Inorganic Chemistry, AGH University of Science and Technology, A. Mickiewicza Av. 30, 30-059 Krakow, Poland

it is important to consider the thermal and chemical properties of described composites. Oxidation resistance and thermal expansion coefficient are the main factors of working temperatures and depend on ceramic phase concentration in manufactured materials. That is why there is a growing number of publications concerning both properties [12, 19].

Up-to-date research has shown a considerable risk of carbide dissolution in metal matrix and/or creation of undesired, topologically close-packed (TCP) phases in the microstructure of obtained composites. To prevent this from happening, two different approaches can be applied. The first one assumes using production methods that are highly controllable in terms of parameters. Thus reaction bed is not reaching the temperature that results in ceramic particles dissolution. Laser-based additive manufacturing is a good example of a valid technology [20, 21]. The other approach assumes high-temperature grow with a relatively short processing time. This prevents excessive interaction between both phases. Spark plasma sintering (SPS) is an exemplary method [22]. Both technologies, give the possibility to process the materials with a speed from  $1.5^{\circ}\text{Cs}^{-1}$  to  $1000^{\circ}\text{Cs}^{-1}$  [23, 24]. Such rapid processes allow carbides to prevail in the metal matrix. Materials obtained in this way typically possess improved hardness or microhardness, when compared to their base alloys.

With that being said, there is a recurring issue of laser processing regarding advanced materials. Successively built-up layers thermally modify deeper ones and lead to the solubility of fine transition metal carbides. Therefore, each layer will have different properties. This tendency is true for both composites and alloys [25]. On the other hand, sintering techniques allow using high heating rates and high pressures across the whole material. The problem in this situation is that the sintering temperature of carbide particles is higher than the Inconel phase. In most cases, it exceeds the melting temperature of the metal. Our research experience shows that this problem can be solved by the hot rolling process following spark plasma sintering [17].

The aim of this study was to obtain  $(\text{Ti,Zr})\text{C}_{0.85}$ -reinforced Inconel 625 by spark plasma sintering as a production method, evaluate its phase composition with microstructure, and verify its applicability by comparison of thermal properties and oxidation resistance to a base superalloy. Mixed carbides, containing Ti, Ta, V, Hf, and other transition metals, show higher hardness than binary system carbides [26]. Some of them have full solubility of constituent carbides but at lower temperatures, their immiscibility appears. Such a situation happens also in the case of  $(\text{Ti,Zr})\text{C}$  phase [26, 27]. On the one hand  $(\text{Ti,Zr})\text{C}$  can be metastable and unstable depending on temperature decomposing to  $\text{TiC}$  and  $\text{ZrC}$ . On the other hand, the initial stages of phase separation around  $1300^{\circ}\text{C}$  can lead to improvement of the material hardness. Therefore, such material decomposition can be used for the

enhancement of the coating's properties. The nanoindentation studies show that this compound can be in a super hard phase [27], and after decomposition will show lamellar structure. Such lamellar structure will be composed of Ti-rich and Zr-rich  $(\text{Ti,Zr})\text{C}$  phase. That is why this ceramic material, from the structural and mechanical point of view, is worth to be introduced into a superalloy metal matrix. To the authors' knowledge, there is no data available from introducing such a carbide phase into the Inconel matrix, so the presented materials are novel in literature.

## Material and experimental methods

In order to manufacture composites in Inconel 625— $(\text{Ti,Zr})\text{C}_{0.85}$  system the following powders were used: commercially available, 99.0% purity Inconel 625 EuTroLoy 16625 powder synthesized by Castolin Eutectic (Montreal, Canada) and laboratory-made mixed carbide  $(\text{Ti,Zr})\text{C}_{0.85}$ . The standard mass composition, except nickel major element, of nickel alloy is as follows: 20–23% Cr, 8–10% Mo, 3.15–3.85% Nb, < 1.5% Fe, < 1% Co, 0.3–0.5% Si, 0.2–0.5% Mn, < 0.1% Ti, < 0.1% Al, < 0.03% C, bal. Ni. The carbide phase was synthesized in the graphite reactor in argon flow from 99.5% purity  $150\ \mu\text{m}$  Ti metal powder of Goodfellow, 99% purity  $45\ \mu\text{m}$   $\text{ZrH}_2$  (Sigma-Aldrich), and phenol–formaldehyde resin type Novolak of Sarzyna at  $1600^{\circ}\text{C}$ . The laboratory-made powder was characterized by phase composition (X-ray Empyrean diffractometer of PANalytical, Almelo, The Netherlands), helium density (gas pycnometer AccuPyc II 1340 of Micromeritics, Norcross, USA), morphology (PHENOM XL of ThermoFisher Scientific) and grain size distribution (Mastersizer 2000 equipped with apparatus attachment Hydro 2000S of Malvern Instruments, Eindhoven, Netherlands). Obtained titanium zirconium carbide solid solution had  $5.654\ \text{gcm}^{-3}$  helium density and was characterized by the grain size distribution of  $d(0.1)=0.44\ \mu\text{m}$ ,  $d(0.5)=1.50\ \mu\text{m}$  and  $d(0.9)=4.19\ \mu\text{m}$ .  $(\text{Ti,Zr})\text{C}_{0.85}$  morphology is presented in Fig. 1. XRD phase analysis, presented in Fig. 4 shows the diffraction pattern of synthesized titanium zirconium mixed carbide. The phase diffractogram was wide, shifted, and contained asymmetric peaks. Wide peaks indicate fine crystalline-size powder and confirm microscopic observations in Fig. 1. Asymmetric peaks are related to some material decomposition to Ti-rich and Zr-rich carbides with improved hardness [26, 27].

The powders of Inconel and 5, 10, 15, and 20 mass% of prepared carbide were mixed together with 0.5 mass% dextrin additive as a granulation aid. This process was made first in dry conditions, in the rotary mill with the use of iron balls for 24 h. Afterward, the water was added to dissolve dextrin. The powder set and dextrin were manually mixed in a mortar. After drying the powder with dextrin

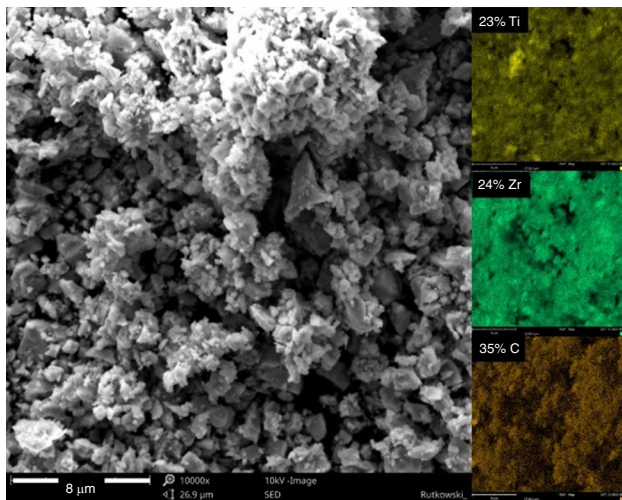


**Fig. 1** Morphology of titanium zirconium mixed carbide

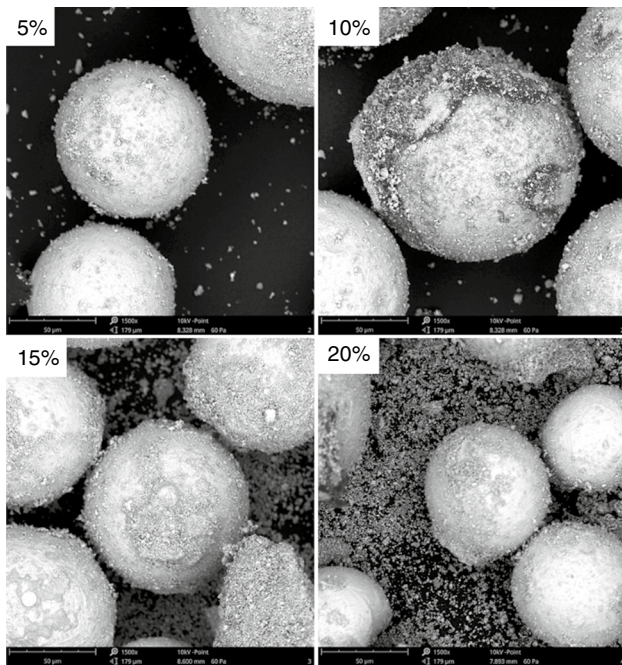


**Fig. 2** Morphology of Inconel 625—x mass% (Ti,Zr)C<sub>0.85</sub> granulates

was granulated in a 125 μm sieve and dried to remove water totally. The morphology of such granulates was observed by scanning electron microscopy (SEM of PHENOM XL of ThermoFisher Scientific) and is presented in Fig. 2.

The prepared granulate powders were subjected to a sintering process by laboratory-made spark plasma sintering apparatus. The used die had a 15 mm diameter and material mass was calculated to obtain 3 mm thick sinters. Based on empiric trials made in temperatures from 950 to 1150 °C,

made on the pure Inconel not to melt material matrix in composite in further examinations, the optimal one was determined to equal 1000 °C. Initially it appeared that too high temperature led to material melting and flow. The heating rate was 100°Cmin<sup>-1</sup> and applied pressure was 45 MPa. The process was conducted in graphite foil separator between graphite elements and the powder. Vacuum was 2•10<sup>-2</sup> mbar and dwelling time in sintering temperature equaled 20 min.

The phase composition of manufactured, dense materials was characterized by X-ray diffractography (XRD). Their density was estimated by the hydrostatic method. Microstructure observation of composite sinters was made by optical microscopy Leica model DM 2500 M (Leica Microsystems CMS GmbH, Mannheim, Germany). To obtain images for computer-aided grain size distribution analysis and determination of ceramic phase volume fraction ImageJ software was used [28]. Scanning electron microscopy (SEM) examinations of composites' microstructure with point and area (mapping) element distribution analysis were made by Scanning Electron Microscopy Nova Nano SEM (FEI, Brno, Czech Republic) with Electron Dispersive Analysis (EDAX—AMETEK GmbH, Unterschleissheim, Germany). It was performed on polished and etched for 10 s in 10% Cr<sub>2</sub>O<sub>3</sub> aqueous solution.

Thermal expansion examinations were made by dilatometric measurements using DIL 402C of Netzsch (Germany, Selb). The process was performed in argon flow with 2°Cmin<sup>-1</sup> heating rate. The thermal expansion coefficient (physical) and mean thermal expansion coefficient (technical) were determined. Results of these examinations were used to determine density changes in the function of temperature, which are also needed to determine the thermal diffusivity, specific heat, and thermal conductivity of the materials. Thermal diffusivity was measured by laser flash analysis method on LFA 427 of Netzsch (Germany, Selb). Measurements were conducted in argon flow and the Capellehman model was used for calculation. The specific heat capacity of SPS-ed series of materials was determined with Netzsch Proteus software with the use of a comparative method to Inconel 600 reference material. Thermal conductivity in a function of temperature was calculated by multiplication of thermal diffusivity, specific heat capacity, and material density.

The obtained materials were also analyzed in terms of their oxidation resistance. Three different examinations were prepared: dynamic one-cycle DSC-TG measurement, dynamic three-cycle DSC-TG measurement, and isothermal oxidation process in a tube furnace for 48 h, which was established to be an optimal time in last our paper [29]. DSC—TG analyses were made by STA 449 F3 Netzsch (Germany, Selb) apparatus equipped with Netzsch Proteus software. Each measurement was made with 10°Cmin<sup>-1</sup> heating rate to 800 °C temperature in 80 mL min<sup>-1</sup> synthetic

air flow in alumina crucibles. Cooling rate was  $40\text{ }^{\circ}\text{C min}^{-1}$ . The same conditions were applied to the three-cycle analysis. For isothermal investigations of material oxidation resistance samples were placed into a tube furnace of Czylok company and the process was performed at  $800\text{ }^{\circ}\text{C}$ , while temperature was reached with  $10^{\circ}\text{Cmin}^{-1}$  heating rate.

Because of preliminary made optical observation and recorded inflections on a dilatometric curve, all of the samples after dilatometric measurements were taken under scanning electron microscopy observation. Also after one and three oxidation resistance cycles oxidation made by the STA analyzer the after-process materials surfaces were investigated by SEM/EDS and confocal microscopy. For this purpose scanning electron microscopy NOVA NANO SEM 200 with Energy Dispersive Spectroscopy (EDS) of EDAX and confocal microscopy by Olympus Lext OLS4000 were made. The confocal microscopy gave the 3D profile of the oxidized surface including Ra and Rz roughness parameters measured by 10 lines. The selected isothermally 48 h oxidized materials were subjected to a surface analysis. The oxides on the material surface were taken to phase analysis by the parallel beam at a sliding angle using GID (Grazing Incidence Diffraction at Empyrean diffractometer of PANalytical company). In order to confirm the formation of oxide phases during the corrosion tests, the Raman spectroscopy was made on selected materials in specified places of the oxidized surface. For this purpose, the Raman Witec Alpha 300 M+ spectrometer was used.

## Results and discussion

### Material densification and phase analysis

The SPS obtained composite materials were hydrostatically measured in order to calculate their apparent density, which was required for thermal analysis and related density calculations. Theoretical density, needed for the determination of materials densification, was calculated on the base of mixture law. The apparent and relative density values are presented in Fig. 3.

The density results revealed that materials with up to 10 mass% can be promising and possess relative density higher than 97.5%. To high content of carbide phase, which as a pure phase ceramic material can be fully sintered around  $1800\text{ }^{\circ}\text{C}$ , lead to lower density of Inconel matrix composites and increased concentration of high energetic weak boundaries between ceramic grains. The sinters of Inconel 625— $(\text{Ti,Zr})\text{C}_{0.85}$  materials were taken to phase composition analysis using XRD method, and the results are presented in Figs. 4 and 5.

Presented XRD results displayed mainly gamma nickel phase. It can be seen that peaks of the pure mixed carbide

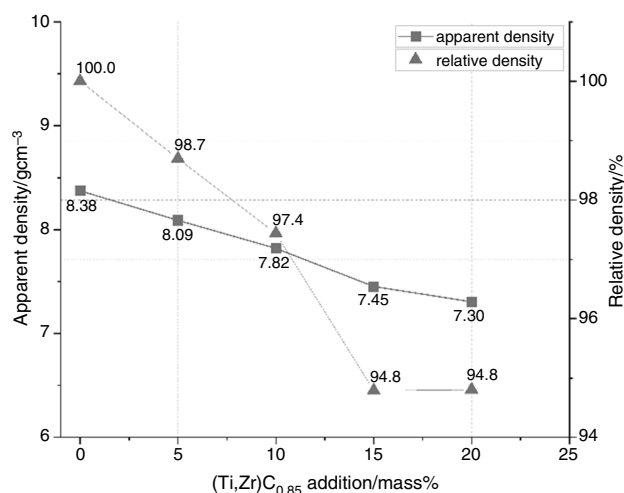


Fig. 3 Inconel 625—mixed carbide densification after SPS process

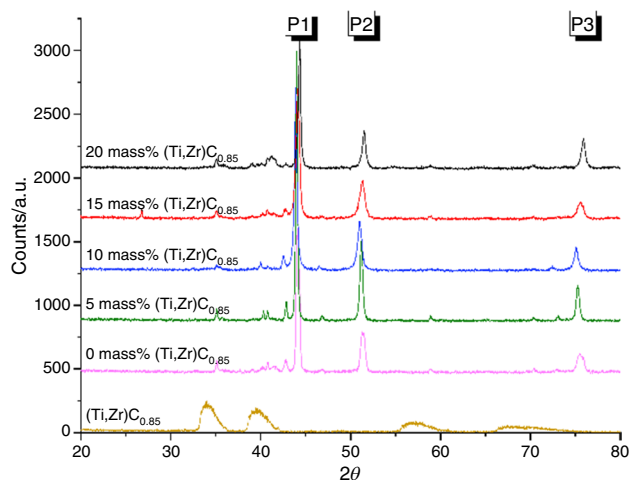
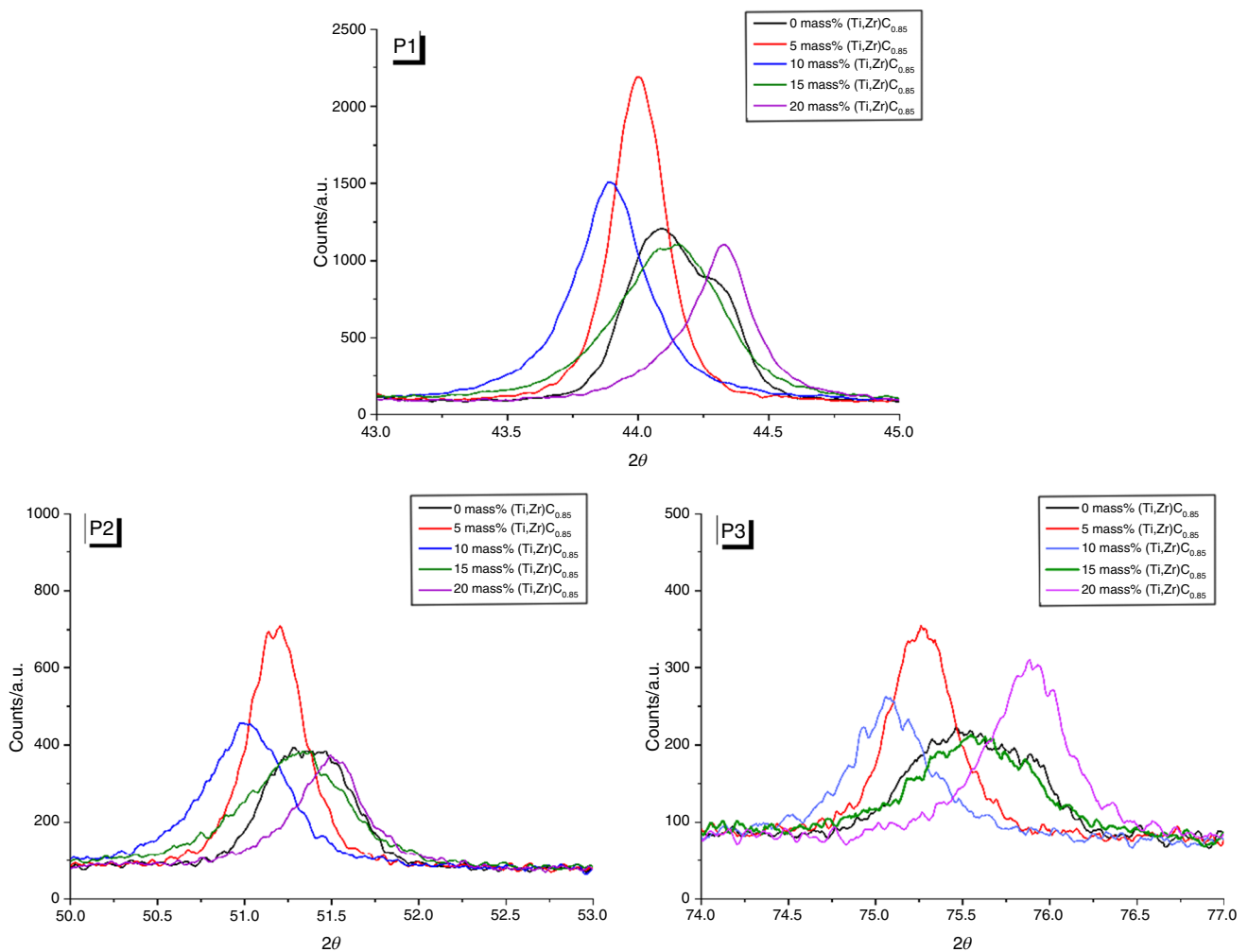


Fig. 4 XRD analysis of Inconel 625— $(\text{Ti,Zr})\text{C}_{0.85}$  materials and pure mixed carbide powder

phase introduced to the nickel alloy were wide. Therefore, particles were fine and disappeared in the composite patterns recorded by XRD. Perhaps this could be due to the formation of a new mixed carbide, which was a solid solution of carbon in the metal matrix, or diffusion of some elements from Inconel, such as niobium from the Inconel matrix to the carbide phase. This allowed to discuss that diffusion takes place during the SPS process. Also, peaks of introduced carbide can overlap peaks of gamma nickel. In order for further evaluation, EDS analysis was made on the sinters and was discussed in the further part of this paper. It can be visible that the addition of mixed carbide changes peaks in the range between 40 and 43 and around 74 of  $2\theta$ . Peaks of Inconel depending on powder mixture composition shift left (for lower addition of carbide) or right (for higher



**Fig. 5** XRD analysis of Inconel 625—(Ti,Zr)C<sub>0.85</sub> materials—enlargement of Inconel peaks

addition of carbide). It was visible in all of the magnified peaks (P1-3) and can be a confirmation of partial solubility of carbides in the Inconel structure or element diffusion from Inconel to the introduced carbides. It can be noted, that in the range of 45–50 and 50–75 of 2theta, the additional (not of Ni-matrix) peaks were either very small or non-existent. In contrast, they occur often with other similar composites done by additive manufacturing [30–35]. This indicated that the SPS method does not introduce many phases occurring in those ranges. When formed by the addition of carbides, those phases are typically non-desirable TCP phases.

### Structural and microstructural examinations

The SPSed materials were polished and observed by Leica DM 2500 M optical microscope. Microstructure images were recorded in two material directions (parallel and perpendicular to SPS applied force) and afterward taken into volume fraction analysis with the use of ImageJ software.

The analysis was made for 10 images per sample, per each direction. Examples of collected images are shown in Fig. 6 and the results of the analysis are shown in Fig. 7. The black areas in Fig. 6 are introduced mixed carbide.

The computer-aided analysis of the volume fraction of introduced titanium zirconium mixed carbide revealed (Fig. 7) that there is almost no difference between volume fractions in different material directions for up to 10 mass% introduced carbide. That can be explained by solubility and mutual diffusion of elements. In the case of higher addition of the second hard phase, there is a visible influence of applied pressure during the SPS process on volume fraction measured in different material directions. For 15 mass% the ratio of volume fraction in perpendicular to parallel direction was 1.35 and for 20 mass% it was 1.13. It can be noted that in the case of higher carbide additive, material properties can be slightly different depending on investigated material direction. Particle size analysis made on collected images confirmed the size of Inconel particles.

**Fig. 6** Non-etched microstructure of Inconel 625—(Ti,Zr)C<sub>0.85</sub>

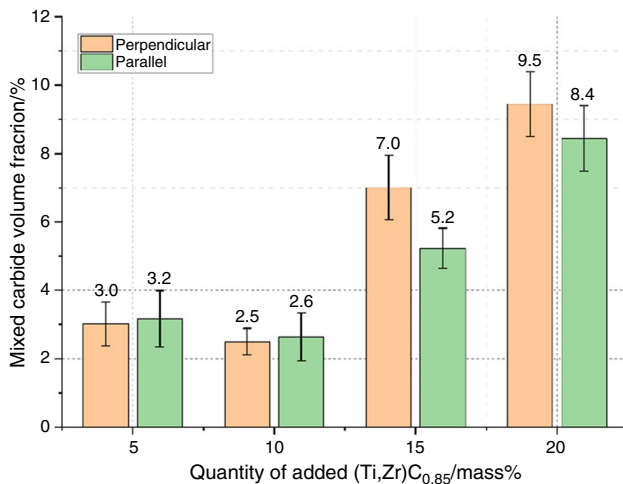
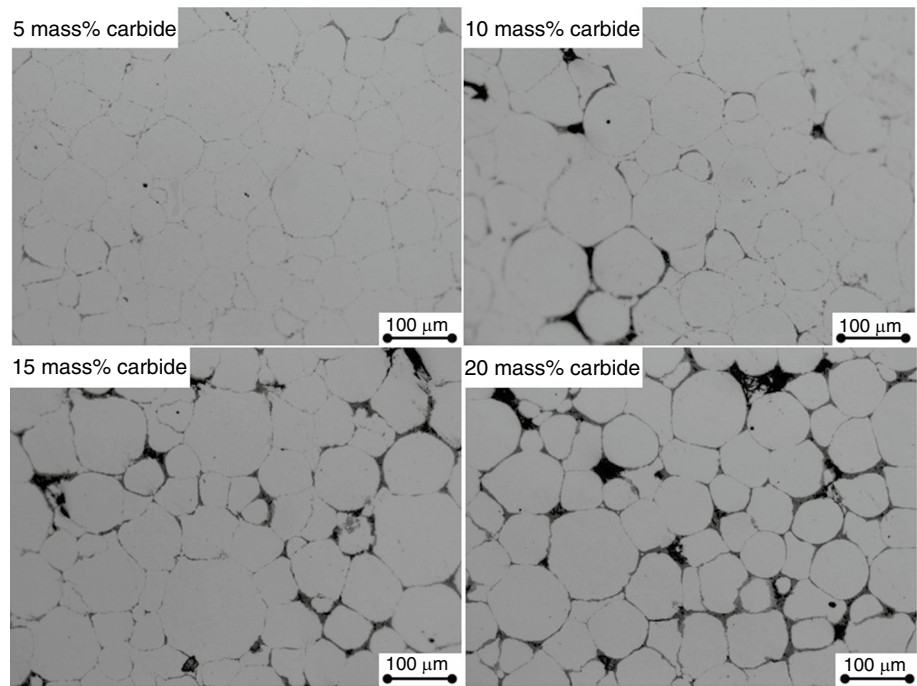


**Fig. 7** Volume fraction of carbides in Inconel 625—(Ti,Zr)C<sub>0.85</sub> materials

Results of SEM observations of etched materials are illustrated in Fig. 8. In order to determine element distribution in the manufactured materials point element distribution and element distribution mapping by EDS method were made and are presented in Figs. 9–11.

The microstructure revealed after etching (Fig. 8) showed that there are slightly smaller dendrites with higher ceramic phase concentration and light precipitates inside the Inconel particle. There was no significant influence of various quantities of added carbide on matrix microstructure but the concentration of the white phase was less visible close to the

border of the ceramic phase. That can be caused by the diffusion of niobium particles from Inconel to the ceramic phase (Figs. 10, 11). The example of chemical analysis made on the etched sample containing 15 mass% of carbide by EDS method showed that particle between matrix grains has different shades of gray. It means they were composed of various elements, not only those initially forming (Ti,Zr)C<sub>0.85</sub>. The point element distribution showed that darker areas consisted of similar content of zirconium and titanium but brighter grains were composed mostly of zirconium. Except for such elements, there is also carbon as an element coming from the carbide phase and nickel with chromium coming from the matrix. Oxygen is a residual element after the material etching process. The dark gray phase (p3 in Fig. 9) in the Inconel particle had typical composition corresponding to the initial Inconel powder. The white places marked by “p4” in Fig. 9 were precipitations rich in niobium and carbon. There are probably mixed carbides.

In order to confirm that there is still mixed carbide present in the matrix, consisting of different elements, mapping process EDS on non-etched, polished material surface was performed (Figs. 10, 11).

Mappings of element distribution showed that nickel and chromium were between Inconel grains in the introduced titanium zirconium carbide zone but in small quantities and are uniformly distributed. What is very important, not noticed during point element analysis is the distribution of niobium element, which normally was a part of precipitations inside Inconel particles. During the SPS process, lots of Nb element diffuses from the external

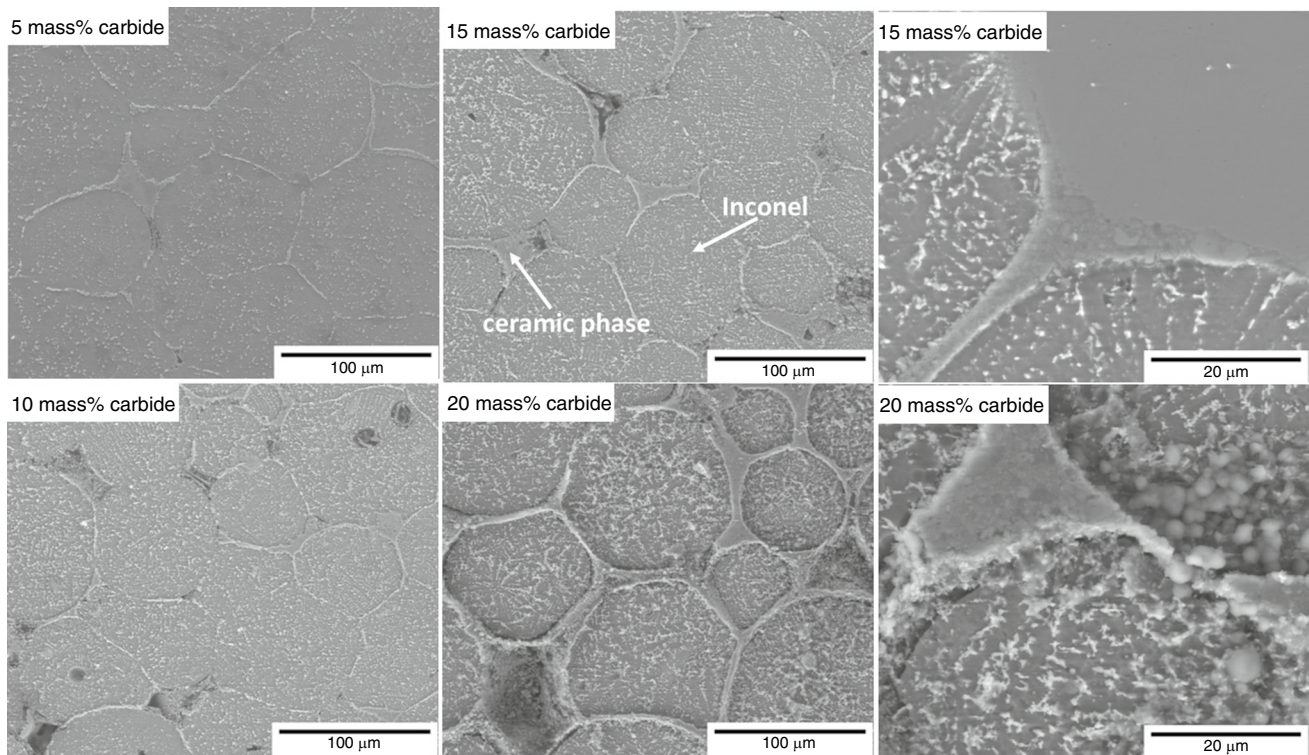
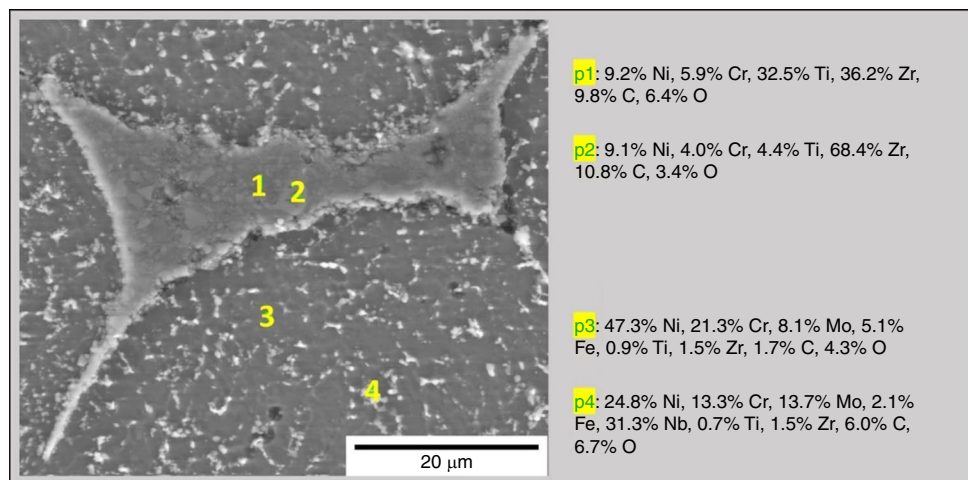


**Fig. 8** Chemically etched microstructure of Inconel 625—(Ti,Zr)C<sub>0.85</sub>

**Fig. 9** Point chemical analysis EDS on the example of Inconel 625—15 mass% (Ti,Zr)C<sub>0.85</sub>



zones of Inconel particles into titanium and zirconium-rich phases. Looking at element distribution maps in the case of 5 and 20 mass% of introduced mixed carbides it can be noticed that zirconium-rich grains contain also a higher concentration of niobium than in the case of places rich in titanium element. The mapping of EDS elements confirms the diffusion of niobium from the near-surface areas of Inconel particles, so they are coming from original niobium precipitations. The EDS analysis confirm also multiphase carbide composition between Inconel matrix

particles so it confirms the lack of (Ti,Zr)C<sub>0.85</sub> peaks in XRD of manufactured composites.

### Thermal analysis of the manufactured composites

After phase, structural and microstructural analysis, obtained composites were subjected to dilatometric measurements to determine material linear changes. The results of the mean thermal expansion coefficient (CTE) were calculated on the base of dilatometric recorded data for three different

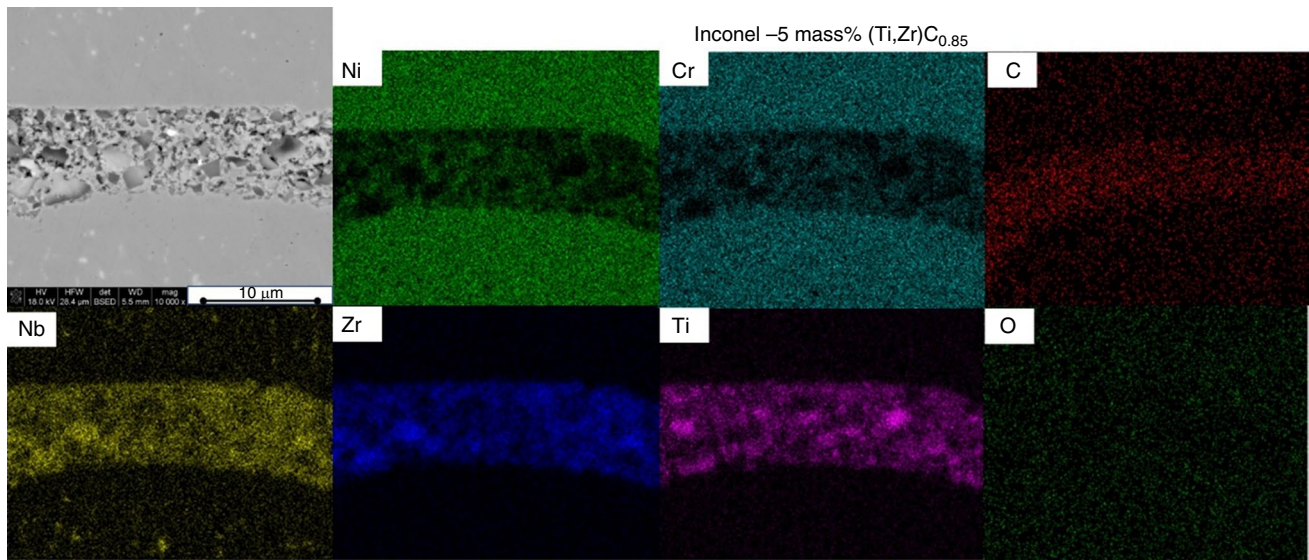


**Fig. 10** Mapping of element distribution in Inconel 625—5 mass% (Ti,Zr)C<sub>0.85</sub> composite

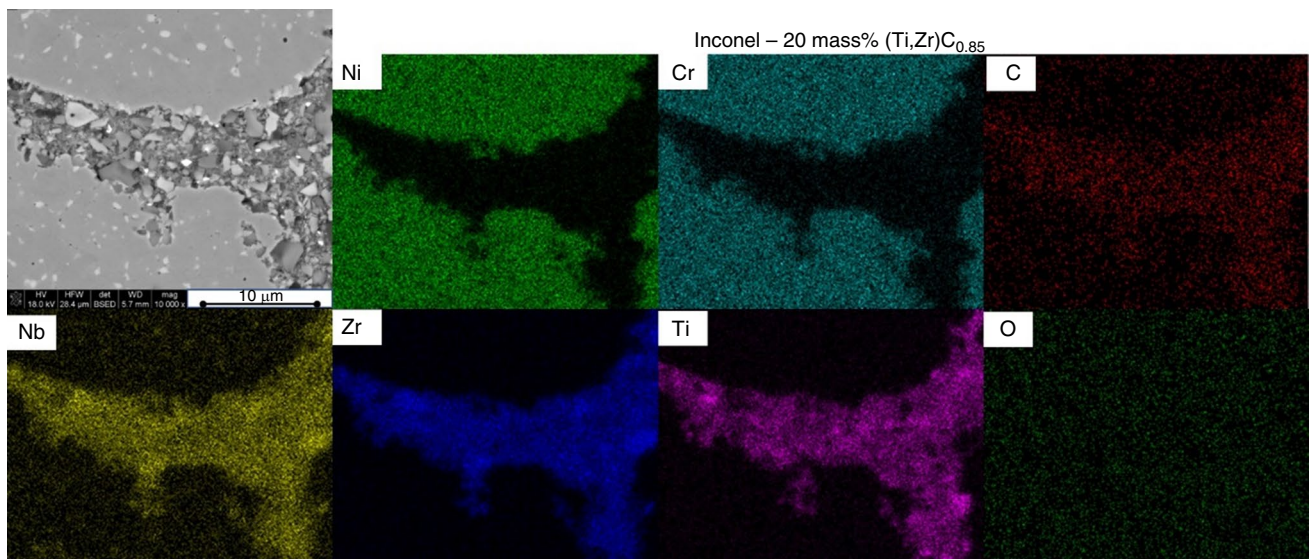


**Fig. 11** Mapping of element distribution in Inconel 625—20 mass% (Ti,Zr)C<sub>0.85</sub> composite

temperature ranges. The mean CTE values versus the content of introduced mixed carbide are presented in Fig. 12. Inconel 625 is used mostly for applications with working temperatures up to 650 °C. The mean thermal expansion coefficient was around  $14.0 \cdot 10^{-6} \text{ K}^{-1}$  and it decreased to  $11.0 \cdot 10^{-6} \text{ K}^{-1}$  for 20 mass% of used mixed carbide for temperatures ranges RT-500 °C. It reached the percolation threshold. Similar tendency was revealed for other determined temperature ranges. For higher temperature mean CTE value of composites exceeded  $17 \cdot 10^{-6} \text{ K}^{-1}$ . The dilatometric process was made with  $2 \text{ K min}^{-1}$  heating rate in argon flow. Such long

measurement was enough for material to undergo oxidation process at temperatures around 550 °C. It was visible by maximal increase in mean CTE for 10 mass% of (Ti,Zr)C<sub>0.85</sub> in temperature ranges above 500 °C. For higher mixed carbide additives mean CTE goes down even to a value below the reference sample which can be connected with carbide thermal expansion.

These values of mean thermal expansion coefficient are very well confirmed by as received data of percentage relative linear changes from dilatometric measurement (Fig. 13). The samples with 10 and 20 mass% of additives show lower



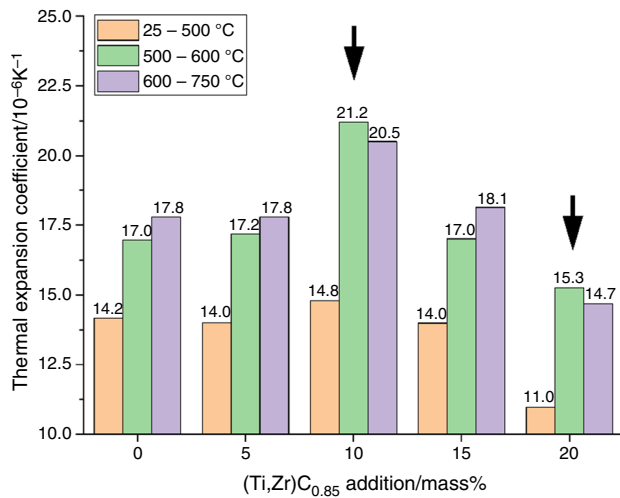


**Fig. 12** Mean thermal expansion coefficient of Inconel 625—(Ti,Zr)C<sub>0.85</sub> materials

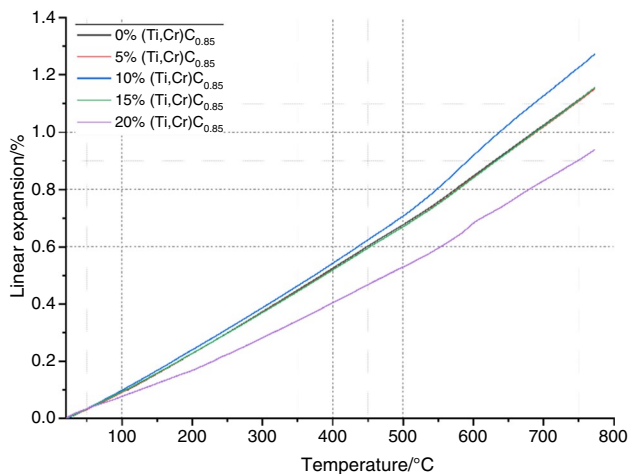


**Fig. 13** Thermal expansion of Inconel 625—(Ti,Zr)C<sub>0.85</sub> materials

or higher thermal expansion which can be also explained by the solubility of transition metal carbides in Ni alloy or diffusion of some elements from Inconel particles to ceramic phase (Figs. 4 and 5). Linear changes in material working temperature range, so up to 650 °C for most of applications are from 0.7 to 1%.

In order to determine the maximal material working temperature the best way is to show the physical alpha curve so the first derivative of the thermal expansion curve according to the temperature—results are presented in Fig. 14. Results showed that this temperature was 500 °C and this process lasted up to temperature maximum 600 °C.

The dilatometric thermal expansion data, described earlier in this paper, allowed calculating changes in the material density in the function of temperature, which is required

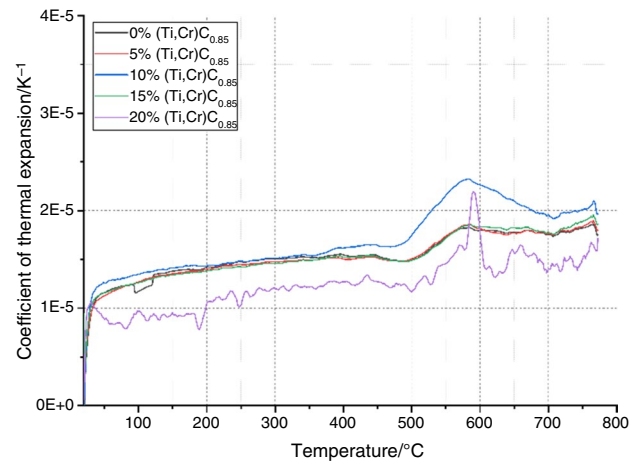


**Fig. 14** Thermal expansion coefficient change in function of temperature of Inconel 625—(Ti,Zr)C<sub>0.85</sub> materials

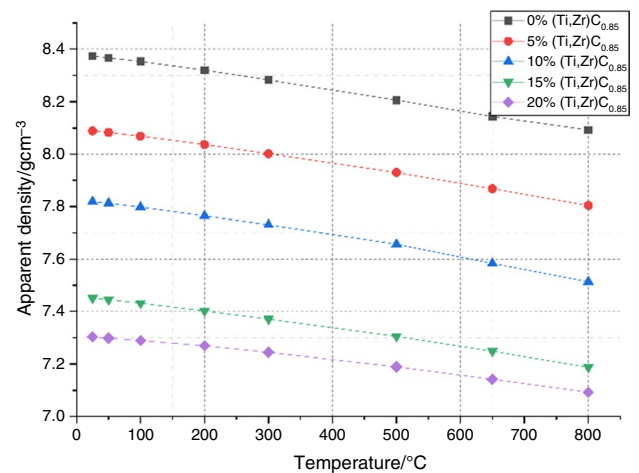


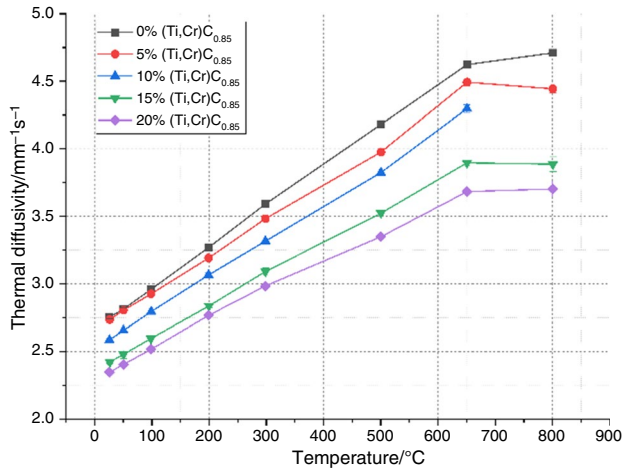
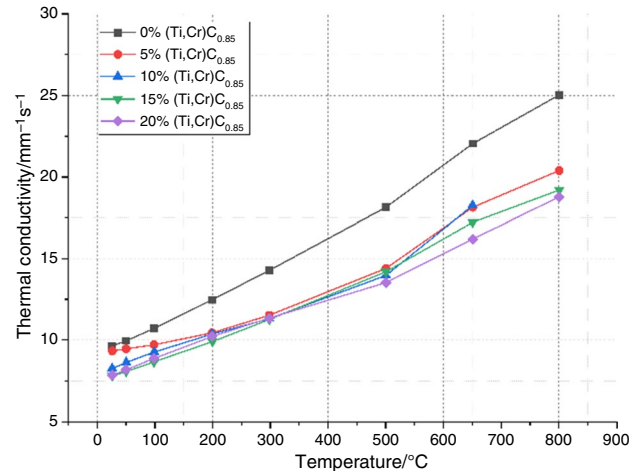
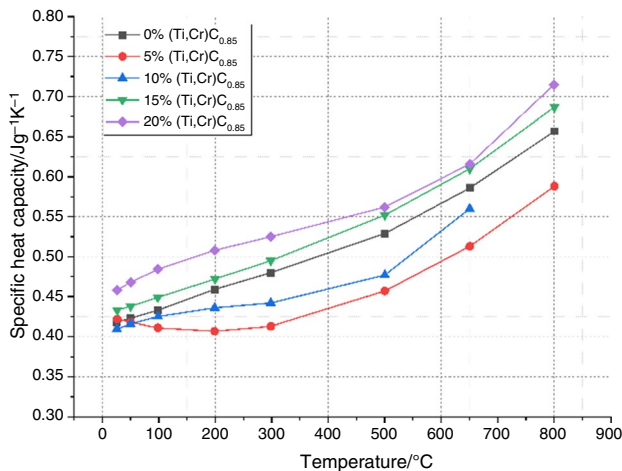
**Fig. 15** Apparent density changes in function of temperature of Inconel 625—(Ti,Zr)C<sub>0.85</sub> materials

for thermal conductivity calculations. The density decreases versus the content of mixed carbide additive and with an increase in temperature. The tendency and slope of density changes in the function of temperature were similar for all of the samples. The fitted mathematical functions to density change points on the curve in Fig. 15 are collected in Table 1.

The required and direct parameter from laser flash analysis made on the Inconel 625—(Ti,Zr)C<sub>0.85</sub> composites is thermal diffusivity and the results are presented in Fig. 16. The results of specific heat capacity calculations are presented in Fig. 17. Due to heat transport by mostly by electrons the thermal diffusivity increases with temperature and slows down around 700 °C. The addition of carbide decreased thermal diffusivity due to phonon–phonon scattering and phonon–electron scattering. The ceramic fine

**Table 1** Mathematical function fitting to density and material thermal properties

(Ti,Zr) C <sub>0.85</sub> / mass%	Density/gcm <sup>-3</sup>	Thermal diffusivity/mm <sup>2</sup> s <sup>-1</sup>	Thermal conductivity/Wm <sup>-1</sup> K <sup>-1</sup>
0	$\rho = 8.385 - 3.298E-4 \cdot T - 4.914E-8 \cdot T^2$	$a = \exp(0.970 + 0.001 \cdot T - 6.381E-7 \cdot T^2)$	$\lambda = 9.308 + 0.013 \cdot T + 1.42E-5 \cdot T^2 - 7.04E-9 \cdot T^3$
5	$\rho = 8.097 - 2.831E-4 \cdot T - 1.050E-7 \cdot T^2$	$a = \exp(0.971 + 0.001 \cdot T - 5.507E-7 \cdot T^2)$	$\lambda = 9.459 - 0.016 \cdot T + 3.33E-5 \cdot T^2 - 1.77E-8 \cdot T^3$
10	$\rho = 7.826 - 2.680E-4 \cdot T - 1.537E-7 \cdot T^2$	$a = \exp(0.933 + 0.001 \cdot T - 2.863E-7 \cdot T^2)$	$\lambda = 7.763 + 0.019 \cdot T - 4.31E-5 \cdot T^2 + 5.85E-8 \cdot T^3$
15	$\rho = 7.458 - 2.577E-4 \cdot T - 9.961E-8 \cdot T^2$	$a = \exp(0.849 + 0.001 \cdot T - 5.986E-7 \cdot T^2)$	$\lambda = 7.646 + 0.008 \cdot T + 1.55E-5 \cdot T^2 + 9.62E-9 \cdot T^3$
20	$\rho = 7.308 - 1.789E-4 \cdot T - 1.136E-7 \cdot T^2$	$a = \exp(0.824 + 0.001 \cdot T - 5.554E-7 \cdot T^2)$	$\lambda = 7.469 + 0.015 \cdot T - 1.27E-6 \cdot T^2 + 1.40E-8 \cdot T^3$

**Fig. 16** Thermal diffusivity changes in function of temperature of Inconel 625—(Ti,Zr)C<sub>0.85</sub> materials**Fig. 18** Thermal conductivity changes in function of temperature of Inconel 625—(Ti,Zr)C<sub>0.85</sub> materials**Fig. 17** Specific heat capacity changes in function of temperature of Inconel 625—(Ti,Zr)C<sub>0.85</sub> materials

grains located between Inconel particles, due to the high concentration of plat defects (boundaries) and porosity between ceramic grains, increase contact resistance related

to boundaries. Thermal diffusivity decreases with the concentration of ceramic phase and with the increase in porosity/decrease in density of composite. The changes' course of thermal properties values of composites versus temperature had a similar tendency to reference Inconel material. Table 1 contains mathematical functions fitted to thermal diffusivity recorded data. The same table contains thermal conductivity fitted functions. Thermal conductivity (Fig. 18) was calculated by the multiplication of thermal diffusivity, density, and specific heat in the function of temperature. Specific heat was calculated on the base of the LFA comparative method by measurement sample and reference material in the same experimental conditions.

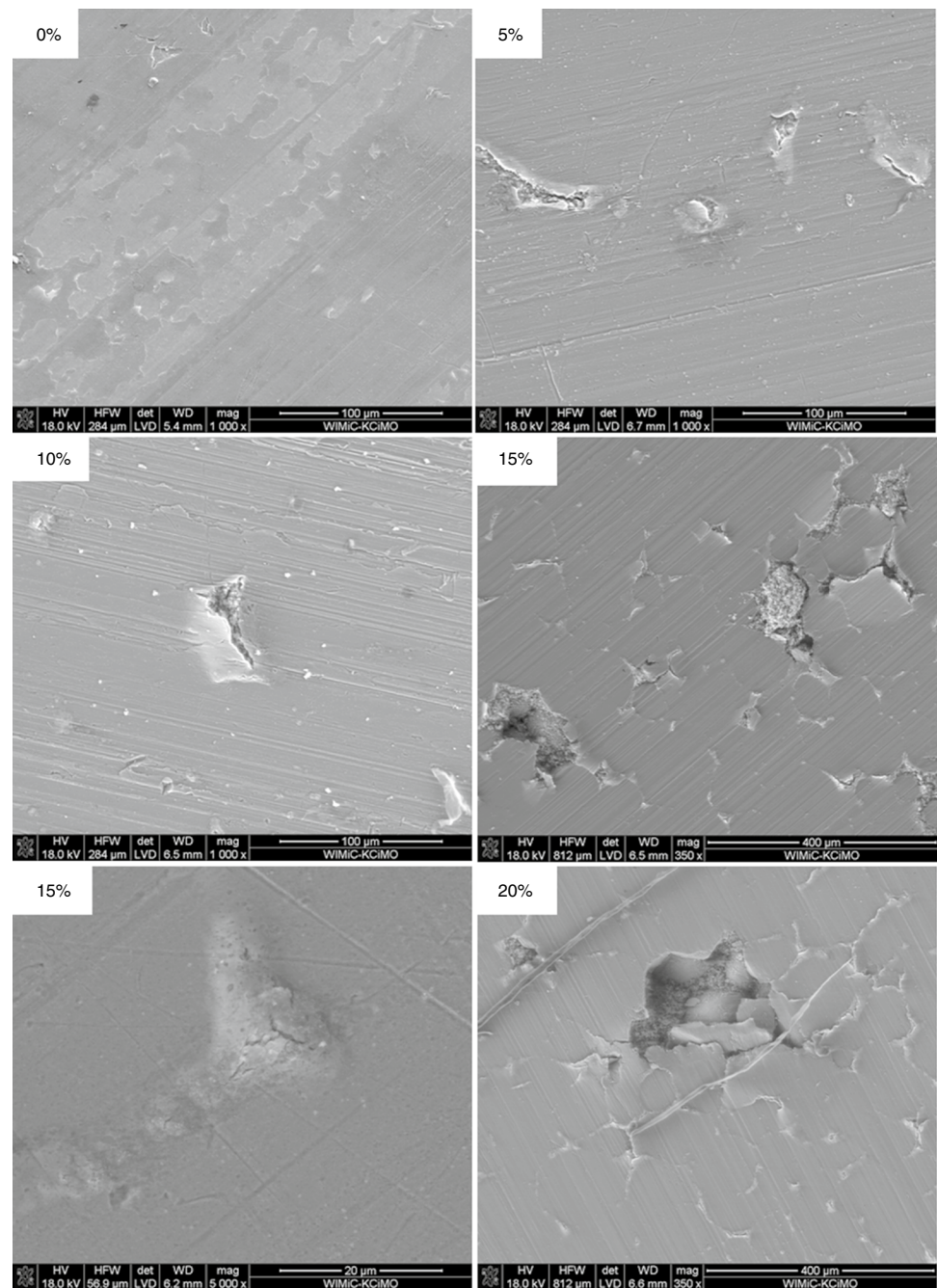
Specific heat capacity in this type of composite strongly depends on carbides' solubility in the metal matrix, and elements diffusion from the metal to carbide, so in fact matrix element change composition was confirmed by XRD peak shifts. Thermal conductivity results shown in Fig. 18 indicate that at room temperature only 5% of carbide additive allows keeping this parameter on the level of reference material. Higher concentrations of introduced ceramic particles lead to a strong decrease in thermal conductivity at room

temperature. For higher ceramic phase concentrations this parameter increases more linearly but there is a lower slope of this change toward Inconel. The increasing addition of mixed carbide also significantly decreases thermal conductivity at elevated temperatures, which can have a significant influence in post-SPS processing surface laser treatment. Those results are similar to the ones obtained by us for the Inconel 625—NbC [36].

## Oxidation resistance analysis

The after-dilatometric process samples were taken for microscopic observations to show what happened with the oxide layer or during the oxidation process at high temperatures, that took place during the measurement process with a low heating rate. They were made by electron scanning microscopy and are illustrated in Fig. 19. The images taken from SEM observations (Fig. 19) show that reference Inconel 625 forms protecting oxide layer at high temperatures. This layer is stable without cracks. The situation changes when mixed

**Fig. 19** Microscopic observation of Inconel 625—(Ti,Zr) C0.85 materials after thermal expansion measurement in the argon flow

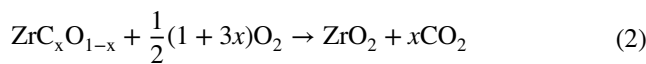
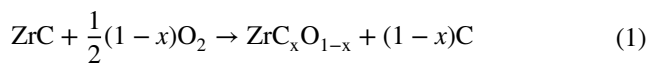


carbide is added to the material—the images of composites with 5–15 mass% of the introduced second phase. In high temperatures material begins to swell on the border between Inconel grains, where are mixed carbide particles. The SEM images of the composites' surface, presented in Fig. 19, show that carbide particles located in between Inconel 625 grains cause the breaking of the passivation layer in higher temperatures and further oxidation process. Probably it is caused by the difference in the thermal expansion coefficient of constituent phases, increase oxide volume during heating up, or faster shrinkage of the matrix toward to oxide layer during the cooling down step.

As is seen in Fig. 19 with 20 mass% of mixed carbide there are exposed not sintered ceramic additive grains, which are very fine, with high surface energy, and can easily react with oxygen increasing oxidation progress. This material behavior is presented and explained by thermal analysis supported with confocal microscopy. In order to evaluate of influence of mixed carbide on Inconel 625 thermal stability the DSC-TG analysis was performed in dynamic conditions in 1-and 3-cycle measurement processes. The 3 cycle step was performed to give information about passive layer stability in dynamic cyclic conditions. The results of single-step DSC-TG analysis are illustrated in Figs. 20–25, including analysis of pure mixed carbide powder shown in Fig. 25.

Data presented in Fig. 20 show that the addition of mixed carbide above 5 mass% strongly increases the kinetics of the oxidation process at a temperature above 350 °C which was visible on dilatometric measurement even in argon flow at 500 °C at low heating rate. The materials with up to 5 mass% of carbides can be used up to 550–600 °C, so even up to working temperatures. Higher additives of mixed carbide shift down onset oxidation temperature by 200 °C to 350 °C. This oxidation step finishes at 600 °C. There is also second step from 700 °C which also depends on carbide concentration and distribution. Analysis of pure mixed carbide powder, presented in Fig. 25, confirm that in composites 350 °C onset temperature is connected with onset of the carbide reaction with oxygen. As can be seen in Fig. 25 this is double step oxidation process, which depends on grain size distribution, and the reaction is very exothermic. This process in the case of pure ceramic powder finishes at 600 °C and the drop of the mass is visible above this temperature, which can be explained by free carbon oxidation coming. This carbon comes from the carbide oxidation process as in the case of ZrC in the temperature range 380–600 °C, which was explained by Gasparrini [37] and Eqs. (1) and (2). This decrease in carbide mass above 600 °C is a confirmation of the same effect shown in the case of composites in Fig. 20. Roma [38] confirmed oxidation onset temperature

and diffusion of oxygen through the formation of the intermediate layer of metal oxycarbide.



Gasparrini claims that residual carbon leaves the material as CO or CO<sub>2</sub>. This confirms a mass decrease in all of the recorded thermogravimetric curves at higher temperatures. The second increase of composite mass during the oxidation process can be attributed to carbide or Inconel corrosion in deeper layers of the materials especially when cracks in the oxide layer are generated.

This behavior of the material and the kinetics are well presented by 1st derivative of thermogravimetric measurements (Fig. 21). First derivative strongly divides oxidation into two steps and its value rapidly increases with mixed carbide concentration. The mass change, illustrated in Fig. 24 shows the “S” shape of the curve, so oxidation slows down for very high carbide concentrations. It is also confirmed by calculated reaction heat which has the highest increase rate for 15 mass% of carbide (Fig. 23). This is also well visible and confirmed by DSC measurements (Fig. 22). The partial explanation or confirmation can be done by confocal microscopy analysis shown in the next part of the paper and by 3 cycles of this process carried by DSC/TG analysis. The three-step oxidation measurement is presented in Fig. 26. The results presented on multicycle measurement confirmed that heating and cooling down steps do not cause cracks and further material oxidation for samples with up to 5 mass% of carbides. A slight increase in the oxide layer was recorded for a high concentration of introduced phases in the second cycle.

Samples, after single and triple-step oxidation analysis, were subjected to confocal microscopy analysis which gave 3D images of the oxidized surface and recorded profile with Ra and Rz material roughness parameters. Images of the material surface are presented in Figs. 27–30 on the example of 5 and 20 mass% of introduced carbide. The roughness parameters measured by the use of 10 lines on the analysis material area are presented in Fig. 31.

The confocal microscopy showed that average material roughness Ra is similar for 0 and 5 mass% of mixed carbide additive. It is almost no difference or small negligible decrease of Rz (Mean roughness depth) roughness for 5 mass% in comparison with reference material—which is visible in Fig. 31 in the case of roughness parameters. It changes strongly for 10 mass% of carbide concentration. Ra

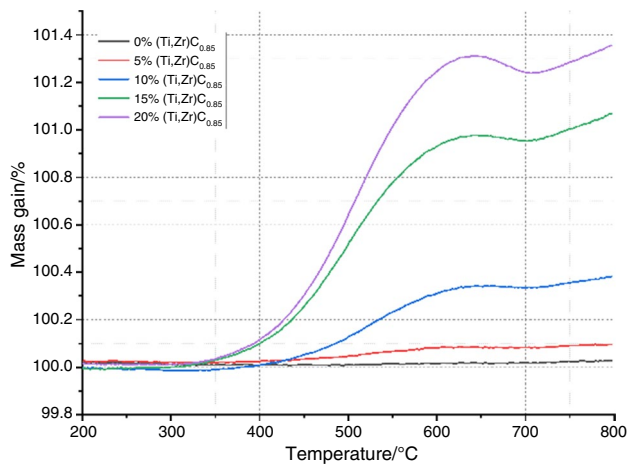


**Fig. 20** Thermogravimetric curves (TG) of Inconel 625—(Ti,Zr)C<sub>0.85</sub> materials

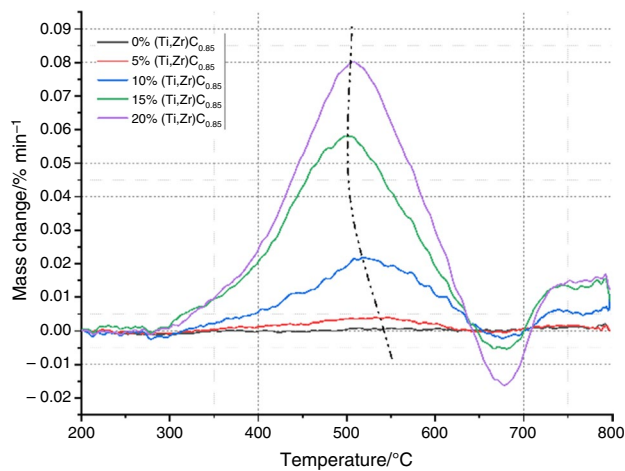


**Fig. 21** First derivative of thermogravimetric curves (DTG) of Inconel 625—(Ti,Zr)C<sub>0.85</sub> materials

and Rz increase after 3 cycles, which can be associated with oxide surface cracking (oxide layer swelling) and opening path for oxygen diffusion. The formed oxide layer can crack during the heating up and cooling downs process steps as a result of thermal expansion mismatch of oxide and substrate or as the increase of oxide volume in areas between Inconel grains. For 15 and 20 mass% of added ceramic phase the difference between 1 and 3 oxidation cycles decreases for both roughness parameters. For 20% values of the introduced ceramic phase, the material's surface profile is slightly lower than for 15%. Such rapid and deep oxidation can be connected with porosity, oxide layer cracking, and high surface energy of not densified/sintered ceramic phase. It is also well visible after surface 3D image analysis made by confocal microscopy. Figures 27 and 28 show almost similar surfaces after 1 and 3 cycles in the case of 5 mass% of

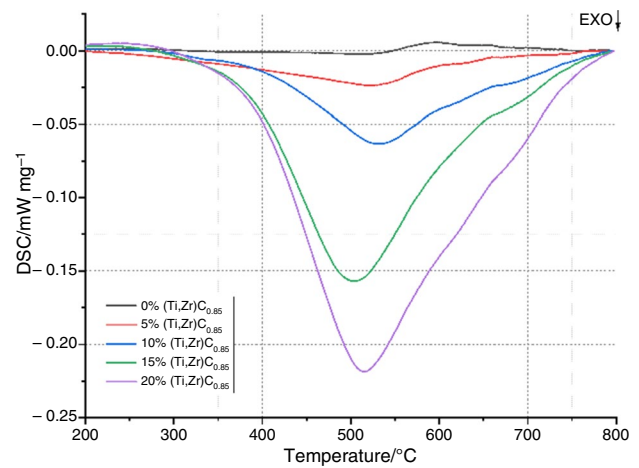


**Fig. 22** DSC curves of heat flow of Inconel 625—(Ti,Zr)C<sub>0.85</sub> materials

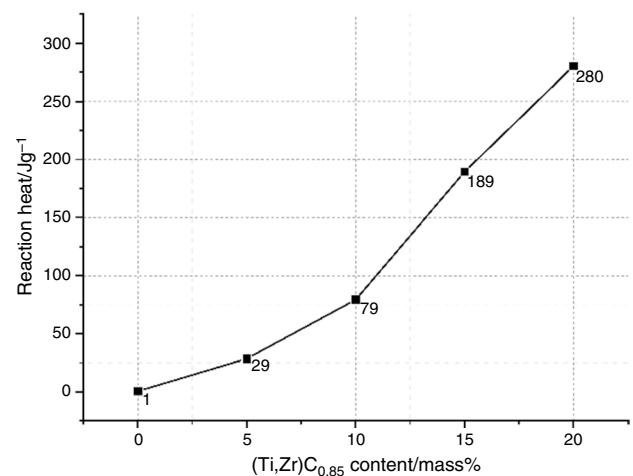


**Fig. 23** Reaction heat calculated from thermal analysis of Inconel 625—(Ti,Zr)C<sub>0.85</sub> materials oxidation process

added carbide. In case of high 20 mass% concentration of introduced ceramic particles there is a noticeable increase in undulations of the material surface, which results in high Ra value—Fig. 30 and 31.

The oxidized surfaces were taken to SEM microscopy in order to complete information concerning the Inconel surface and ceramic phase, which cannot be determined by a confocal microscope. The results of surface observations are presented in Figs. 32, 33.

In the case of 5 mass% of introduced carbide, presented in Fig. 32, during the oxidation process, as in comparison with dilatometric measurement, the sample shows similar behavior to the Inconel matrix. After the first cycle there are small corrosion less resistant places on the boundaries or in the niobium-based precipitates (marked by arrow)—so such

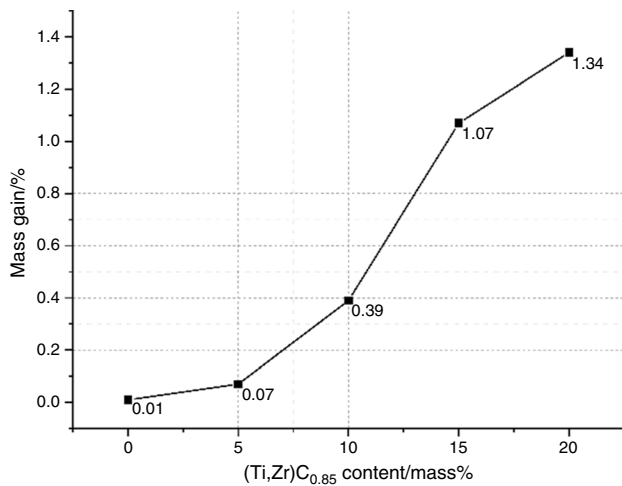


**Fig. 24** Mass gain after 1 cycle oxidation process in dynamic conditions of Inconel 625—(Ti,Zr)C<sub>0.85</sub> materials

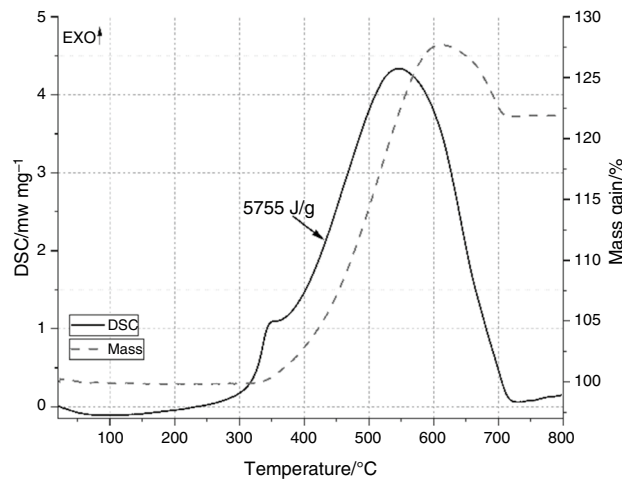


**Fig. 25** DSC-TG curves (Ti,Zr)C<sub>0.85</sub> fine powder used as secondary constituent phase of composites

content of added carbide to the material is a limiting value for material application mechanical and corrosive applications. To keep that material behavior, ceramic particles must be well distributed in the Inconel matrix. In the case of 20 mass% of carbide additive, there is a lot of mixed carbide particles on the boundaries and in the triple point (Figs. 32 and 33). In accordance with SEM/EDS analysis mixed carbides or carbides after the SPS process contain also niobium, nickel, and chromium (Figs. 10 and 11). With accordance to Figs. 22 and 23 there is a very strong exothermic and fast reaction of particles with oxygen which results in volume material changes, cracking connected with a molar volume smaller in comparison with amorphous oxide before crystallization, stresses generation, and finally lower oxidation resistance. The third cycle of heating up and cooling down

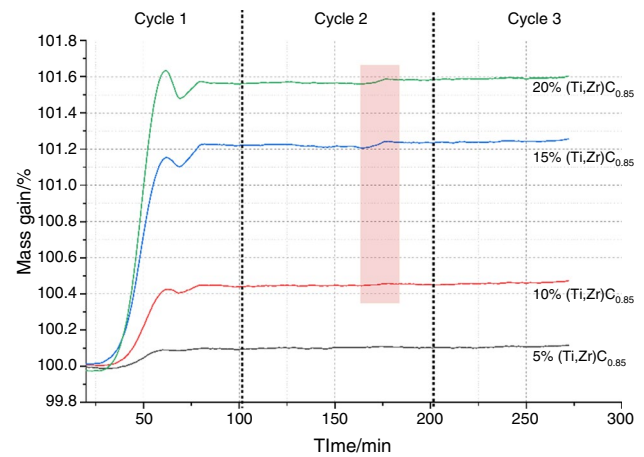


**Fig. 26** Mass gain after 3 cycles oxidation process in dynamic conditions of Inconel 625—(Ti,Zr)C<sub>0.85</sub> materials

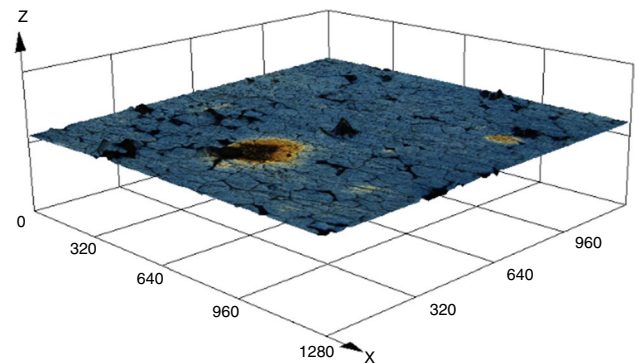


**Fig. 27** Confocal microscopy 3D image of Inconel with 5 mass% of introduced mixed carbide after 1 dynamic cycle of oxidation process up to 800 °C

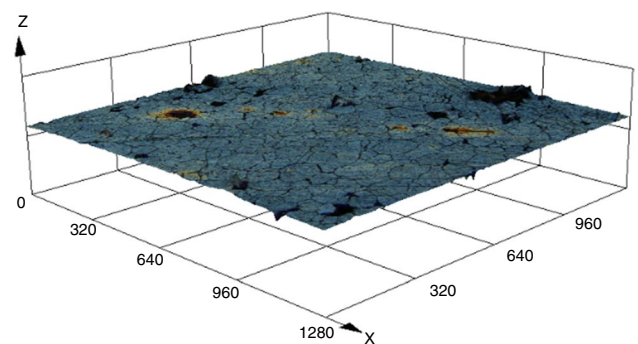


**Fig. 28** Confocal microscopy 3D image of Inconel with 5 mass% of introduced mixed carbide after 3 dynamic cycles of oxidation process up to 800 °C

shows further corrosion of the carbide material and larger paths/possibilities of oxygen diffusion. It is not such strong as in the 1-cycle process due to the decreasing content of the

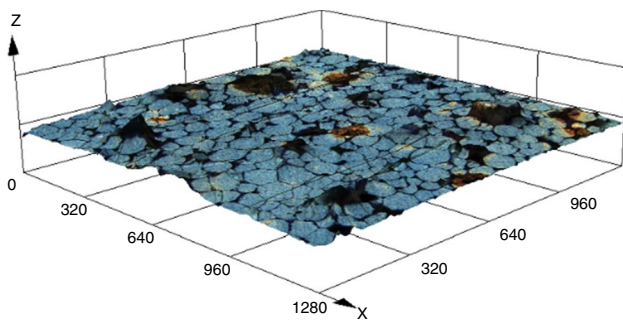


**Fig. 29** Confocal microscopy 3D image of Inconel with 20 mass% of introduced mixed carbide after 1 dynamic cycle of oxidation process up to 800 °C

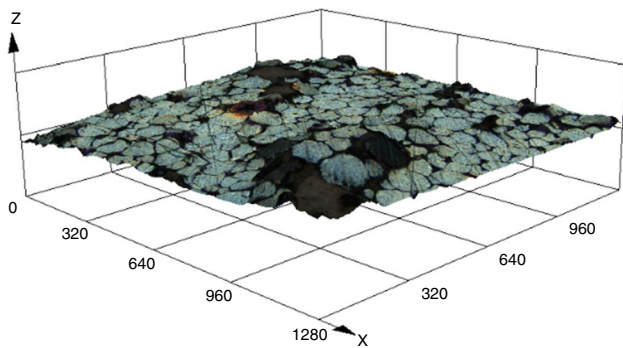


**Fig. 30** Confocal microscopy 3D image of Inconel with 20 mass% of introduced mixed carbide after 3 dynamic cycles of oxidation process up to 800 °C

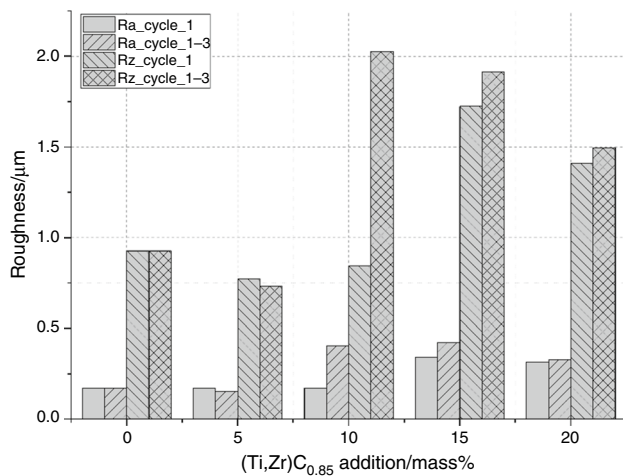


**Fig. 31** Ra and Rz parameters of material surface roughness measured after 1 and 3 oxidation process cycles

residual carbide reactant or the formation of different oxides. It is well visible in Fig. 31 showing roughness parameter values. The point EDS analysis shown in Fig. 33 indicates

two types of oxides: containing mostly Ni and Cr elements (dark places—point 1) and composed of Ti and Zr elements (bright places—point 2). In the matrix, there were recognized gray places containing mostly 70% Ni and 20% Cr, which is typical for pure Inconel, and brighter ones connected with additional precipitates of Zr element. In this composite, a larger amount of oxygen in the case of Ti- and Zr-rich places in the material, which indicates on high material affinity to the oxygen, and what is naturally connected with a high surface energy of fine carbide phase microstructure (SEM image in Figs. 10 and 11).

All of the prepared samples were also taken into an extended time isothermal oxidation process, which took 48 h. Results and comparison of material mass gain after isothermal and dynamic oxidation processes are illustrated in Fig. 34. Obtained data show that most of the oxide is formed during a short time approximately 80 min after the first dynamic corrosion cycle. Afterward the process slows down and small difference between 1 and 3 cycles like in the case of the difference between 3rd cycle and 48 h oxidation time. The oxidation mechanism of added carbides might be contrary to those indicated in [39] as mass gain increases in relation to the amount of carbide addition is increasing. It was similar to our previous study regarding composites [29], and it indicates that up to 10 mass% of added carbide reinforcement, it is competitive to pure 625 superalloys obtained in additive manufacturing processing [40, 41].

In order to recognize what can be formed during oxidation process of Inconel 625—(Ti,Zr)C<sub>0.85</sub> composites the phase composition of oxide layer after 48 h of the process was determined by Grazing Incidence of Diffraction (GID), what is illustrated in Fig. 35.

The XRD/GID analysis data presented in Fig. 35 confirmed formation of various oxide compounds on the nickel alloy surface as an effect of long time oxidation process. On our analysis we found zirconia and titanium based oxides, nickel chromite and chromium titanate. Chromium titanate plays a role similar to CrNbO<sub>4</sub>. It will be formed during material corrosion process [29]. The CrNbO<sub>4</sub> will also be formed in case of niobium precipitation in matrix due to reaction no. 3 or in the area of introduced mixed carbide phase.



The examples of metal matrix composites with introduced 5 and 15 mass% of titanium zirconium mixed carbide confirmed the formation of nickel chromite presented on diffractograms in Fig. 35, what is the standard spinel reaction product during the Inconel oxidation process [36, 42]. Such oxidation process begins at around 800 °C depending on Inconel type (for Inconel 625 it is 767 °C), which can partially explain second increase of material mass recorded

**Fig. 32** SEM/EDS analysis of Inconel 625 based composite with 5 and 20 mass% of added (Ti,Zr)C<sub>0.85</sub> after first oxidation cycle in dynamic conditions

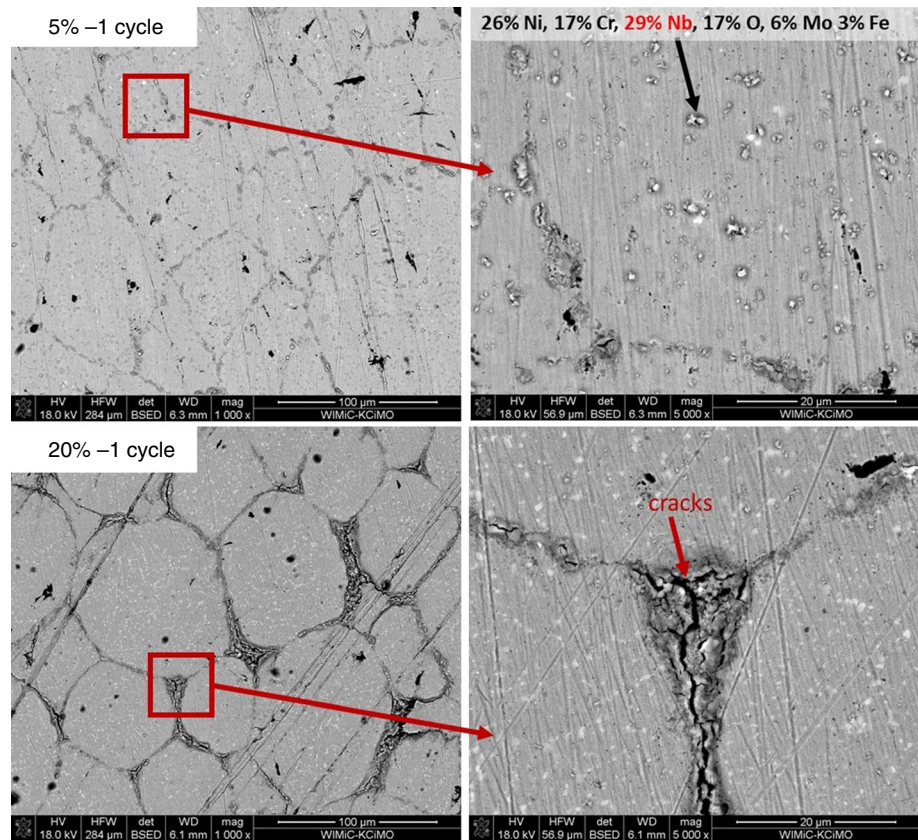
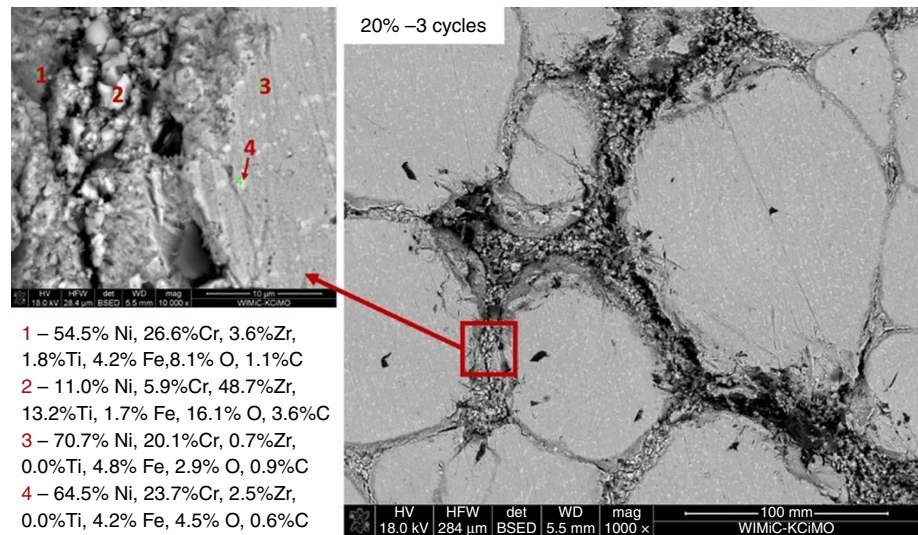


**Fig. 33** SEM/EDS analysis of Inconel 625 based composite with 20 mass% of added (Ti,Zr)C<sub>0.85</sub> after third oxidation cycle in dynamic conditions



during DSC/TG analysis (Fig. 15) [40]. Staszewska explains [43], that Inconel oxidation is an electrochemical process and starts from chromium atom with oxygen reaction forming stable layer on the substrate surface. Then also niobium oxide is formed and both of the oxides play the role of electrolyte. The external layer of the oxidized material surface becomes a cathode and metal coming from Inconel is the

anode. In that way, chromium oxide in a solid state reacts with nickel oxide forming NiCr<sub>2</sub>O<sub>4</sub> spinel—reaction no. 4.



In the case of manufactured composites the following oxide phases were also recorded during XRD analysis (Fig. 35): zirconia, zirconium titanate and chromium



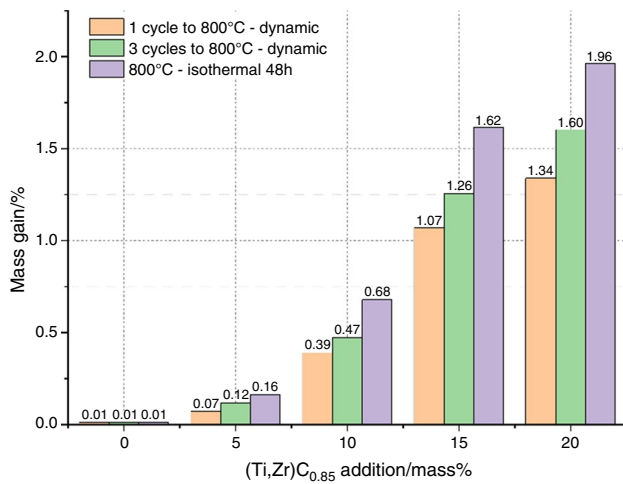


**Fig. 34** Comparison of mass gain changes in function of additive concentration and oxidation process analysis

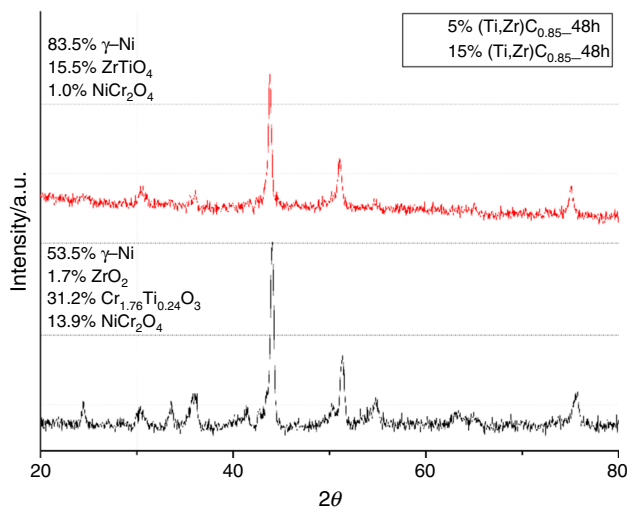
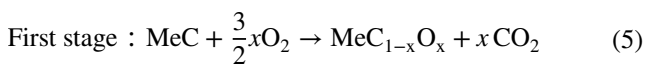
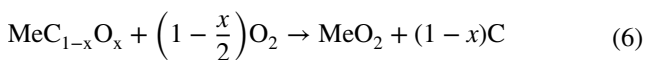


**Fig. 35** GID analysis of oxide layer on the example of 5 and 15 mass% introduced mixed carbide

titanate. Budkiewicz [44] mentioned that Shimada and Kozeki proposed the following reaction stages and equations of oxidation of transition metal carbides:

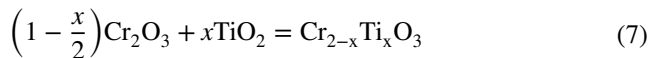


and at second stage:



Such layer of oxide at the beginning is amorphous and after crystallization it becomes porous due to the difference between molar volume. It can explain material cracking and formation of oxygen diffusion path during mixed transition carbides corrosion (SEM images in Figs. 32 and 33). In the last step CO<sub>2</sub> is produced. In case of isothermal process there are only 2 stages—first has parabolic character and second linear kinetic behavior after formation of all layers of oxides. This stage is explained by oxygen diffusion through external to internal oxide layer. In his research, Budkiewicz shows that oxidation of fine titanium carbide starts at about 300 °C and can be move for high heating rate to 400 °C what confirms or DSC/TG analysis of carbide powder. In case of dense carbide ceramic (hot pressed) oxidation can start at higher temperatures about 700–800 °C as in the case of titanium carbide [45].

The XRD/GID analysis showed also the formation of chromium titanite. This phase recognized on the diffraction pattern (Fig. 35) was described by Niemayer [46] and is formed according to the following reaction:



In order to confirm XRD analysis of oxidized layer we performed Raman spectroscopy analysis on the oxidized Inconel 625 matrix and composite containing 20 mass% of ceramic phase. The results of the measurement are presented in Figs. 36 and 37.

Results (Fig. 36) confirmed the formation of chromium oxide and nickel chromate as a reaction of Inconel constituent elements with oxygen, which was also confirmed by other papers [36, 42]. Raman spectroscopy analysis of the ceramic phase, present between Inconel 625 grains, indicated the formation of tetragonal zirconia and zirconia titanate (ZrTiO<sub>4</sub>). The formation of these phases is consistent with XRD analysis (Fig. 37, point 5). The Raman spectroscopy also revealed the existence of titania (TiO<sub>2</sub>) and niobium oxide. Titania is a result of the oxidation of introduced titanium zirconium carbide. Niobium oxide was detected in the area between Inconel grains because of niobium diffusion during the SPS process, which was confirmed by EDS mapping analysis (Figs. 10 and 11). The Raman shifts were described and confirmed by literature [47–52]. The peak of ZrTiO<sub>4</sub> is slightly bent on its right side, which can be explained by the non-stoichiometric character of such a compound. Such oxides can be also recognized by the XPS method [53, 54] which will be performed by us in future oxidation experiment in case of carbides introduced to the metal matrix.

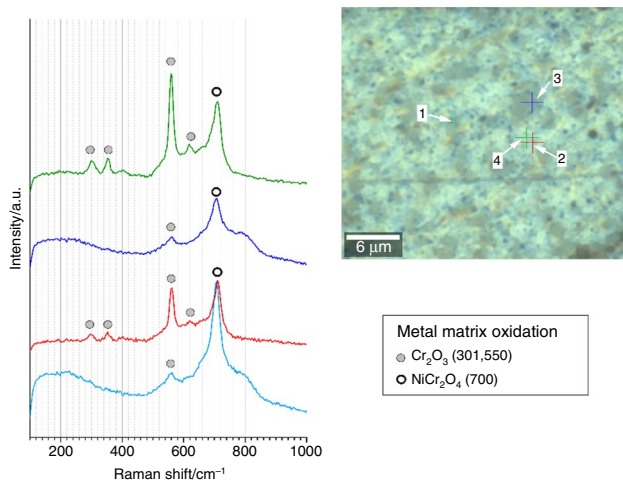


**Fig. 36** Raman spectroscopy analysis of oxidized Inconel 625 grain

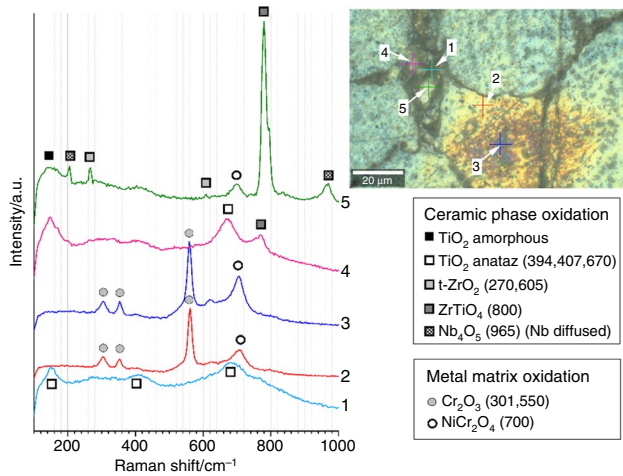


**Fig. 37** Raman spectroscopy analysis of oxidized Inconel 625 with introduced 20% carbide

## Conclusions

- Only samples with up to 5 mass% can be used as material mechanical reinforcement without a remarkable decrease in oxidation resistance.
- Above 5 mass% of introduced carbides oxidation process begins to be rapid and there are visible significant mass gains. The onset temperature of the process moves from 550 to 350 °C.
- Cracking of the passive oxide layer can be made because of thermal expansion coefficients differences of material constituent phases, different volumes of various oxides formed during the oxidation process, the different molar volumes of crystallized oxides toward to amorphous oxide layer, and initial carbide.

- The value of thermal diffusivity and thermal conductivity decreases at room and elevated temperatures with increasing content of introduced mixed carbides and densification changes.
- For all composite materials, thermal properties (heat transfer) increases in function of temperature.
- Specific heat strongly depends on material composition and carbide solubility in the metal matrix and element diffusion.
- Zirconium coming from mixed carbides can be mostly responsible for worse resistance to oxidation of manufactured composites.
- From our experience oxidation resistance can be improved by the hot rolling process, which will be the next step in our research.

**Acknowledgments** The research was supported by the statutory project of the National Science Center No. 16.16.160.557 of the AGH University of Science and Technology in Krakow. We want to thank dr. Maciej Bik from Department of Silicate Chemistry and Macromolecular Compounds of Faculty of Materials Science and Ceramics AGH UST for help at Raman Spectroscopy measurements.

**Author contributions** Conceptualization was contributed by PR; methodology was contributed by PR; formal analysis and investigation were contributed by PR, JH, AG, KP, PN, BH; writing was contributed by PR; graphical presentations were contributed by PR; writing—review and editing, was contributed by PR, JH, AG; resources were contributed by PR; supervision was contributed by PR, DK.

**Open Access** This article is licensed under a Creative Commons Attribution 4.0 International License, which permits use, sharing, adaptation, distribution and reproduction in any medium or format, as long as you give appropriate credit to the original author(s) and the source, provide a link to the Creative Commons licence, and indicate if changes were made. The images or other third party material in this article are included in the article's Creative Commons licence, unless indicated otherwise in a credit line to the material. If material is not included in the article's Creative Commons licence and your intended use is not permitted by statutory regulation or exceeds the permitted use, you will need to obtain permission directly from the copyright holder. To view a copy of this licence, visit <http://creativecommons.org/licenses/by/4.0/>.

## References

1. Chintala A, Tejaswi Kumar M, Sathishkumar M, Arivazhagan N, Manikandan M. Technology development for producing Inconel 625 in aerospace application using wire arc additive manufacturing process. *J Mater Eng Perform*. 2021. <https://doi.org/10.1007/s11665-021-05781-6>.
2. Gupta RK, Anil Kumar V, Gururaja UV, Shivaram BRNV, Maruti Prasad Y, Ramkumar P, Chakravarthi KVA, Sarkar P. processing and characterization of Inconel 625 nickel base superalloy. *Mater Sci Forum*. 2015. <https://doi.org/10.4028/www.scientific.net/MSF.830-831.38>.
3. Karmuhilan M, Kumanan S. A review on additive manufacturing processes of Inconel 625. *J Mater Eng Perform*. 2021. <https://doi.org/10.1007/s11665-021-06427-3>.

4. Shoemaker LE. Alloys 625 and 725: trends in properties and applications, superalloys 718, 625, 706 and derivatives. USA: The Minerals, Metals & Materials Society; 2005.
5. Vesel A, Drenik A, Elersic K, Mozetica M, Kovac J, Gyergyek T, Stockel J, Varju J, Panek R, Balat-Pichelin M. Oxidation of Inconel 625 superalloy upon treatment with oxygen or hydrogen plasma at high temperature. *Appl Surf Sci.* 2014. <https://doi.org/10.1016/j.apsusc.2014.03.160>.
6. Parizia S, Marchese G, Rashidi M, Lorusso M, Hryha E, Manfredi D, Biaino S. Effect of heat treatment on microstructure and oxidation properties of Inconel 625 processed by LPBF. *J Alloy Compd.* 2020. <https://doi.org/10.1016/j.jallcom.2020.156418>.
7. Solecka M, Rutkowski B, Kopia A. Kinetics of the high temperature oxidation of the Inconel 686 coatings in the waste incineration ash. *Arch Metall Mater.* 2021. <https://doi.org/10.24425/ams.2021.139437>.
8. Pratheesh Kumar S, Elangovan S, Mohanraj R, Ramakrishna JR. A review on properties of Inconel 625 and Inconel 718 fabricated using direct energy deposition. *Mater Today- Proc.* 2021. <https://doi.org/10.1016/j.matpr.2021.02.566>.
9. Verdi D, Garrido MA, Múñez CJ, Poza P. Mechanical properties of Inconel 625 laser clad coatings: depth sensing indentation analysis. *Mater Sci Eng A.* 2014. <https://doi.org/10.1016/j.msea.2014.01.026>.
10. Tian Z-H, Zhao Y-T, Jiang Y-J, Ren H-P. Microstructure and properties of Inconel 625 + WC composite coatings prepared by laser cladding. *Rare Met.* 2021. <https://doi.org/10.1007/s12598-020-01507-0>.
11. Raahgini C, Verdi D. Abrasive wear performance of laser clad Inconel 625 based metal matrix composites: effect of the vanadium carbide reinforcement phase content. *Surf Coat Tech.* 2022. <https://doi.org/10.1016/j.surfcoat.2021.127975>.
12. Emanuelli L, Molinari A, Pellizzari M. Interaction between WC and Inconel 625 under solid and liquid state sintering conditions. *Metals-Basel.* 2021. <https://doi.org/10.3390/met11040666>.
13. Muvvala G, Karmakar DP, Kumar NA. Monitoring and assessment of tungsten carbide wettability in laser clad metal matrix composite coating using an IR pyrometer. *J Alloy Compd.* 2017. <https://doi.org/10.1016/j.jallcom.2017.04.254>.
14. Shi H, Chai Y, Li N, Yan J, Peng H, Zhang R, Li M, Bai D, Chen K, Liu Z, Luo M, Sun Q, Zhu X, Zhang Y, Li R, Zhang B, Dong X. Investigation of interfacial reaction mechanism between SiC and Inconel 625 superalloy using thermodynamic calculation. *J Eur Ceram Soc.* 2021. <https://doi.org/10.1016/j.jeurceramsoc.2021.02.046>.
15. Bakkar A, Ahmed MMZ, Alsaleh NA, El-Sayed Seleman MM, Ataya S. Microstructure, wear, and corrosion characterization of high TiC content Inconel 625 matrix composites. *J Mater Res Tech.* 2019. <https://doi.org/10.1016/j.jmrt.2018.09.001>.
16. Huebner J, Rutkowski P, Kata D, Kusiński J. Microstructural and mechanical study of inconel 625–tungsten carbide composite coatings obtained by powder laser cladding. *Arch Metall Mater.* 2017. <https://doi.org/10.1515/amm-2017-0078>.
17. Graboś A, Huebner J, Rutkowski P, Zhang S, Kuo Y-L, Kata D, Hayashi S. Microstructure and hardness of spark plasma sintered Inconel 625-NbC composites for high-temperature applications. *Materials.* 2021. <https://doi.org/10.3390/ma14164606>.
18. Zhang B, Bi G, Nai S, Sun Ch, Wei J. Microhardness and microstructure evolution of TiB<sub>2</sub> reinforced Inconel 625/TiB<sub>2</sub> composite produced by selective laser melting. *Opt Laser Technol.* 2016. <https://doi.org/10.1016/j.optlastec.2016.01.010>.
19. Hong Ch. High-temperature oxidation performance and its mechanism of TiC/Inconel 625 composites prepared by laser metal deposition additive manufacturing. *J Laser Appl.* 2015. <https://doi.org/10.2351/1.4898647>.
20. Dinda GP, Dasgupta AK, Mazumder J. Laser aided direct metal deposition of Inconel 625 superalloy: microstructural evolution and thermal stability. *Mater Sci En A.* 2009. <https://doi.org/10.1016/j.msea.2009.01.009>.
21. Abioye TE, Folkes J, Clare AT. A parametric study of Inconel 625 wire laser deposition. *J Mater Process Tech.* 2013. <https://doi.org/10.1016/j.jmatprotec.2013.06.007>.
22. Hakeem AS, Patel F, Minhas N, Malkawi A, Aleid Z, Ehsan MA, Sharrofna H, Al GA. Comparative evaluation of thermal and mechanical properties of nickel alloy 718 prepared using selective laser melting, spark plasma sintering, and casting methods. *J of Mat Res Tech.* 2021. <https://doi.org/10.1016/j.jmrt.2021.03.043>.
23. Zhang Z, Han BQ, Huang JY, Han YH, Zhou Y, Kakegawa K, Lavernia EJ. Mechanical behavior of cryomilled Ni superalloy by spark plasma sintering. *Metall Mater Trans A.* 2009. <https://doi.org/10.1007/s11661-009-9914-1>.
24. Liu H, Tan ChKI, Wei Y, Lim SH, Lee CJJ. Laser-cladding and interface evolutions of inconel 625 alloy on low alloy steel substrate upon heat and chemical treatments. *Surf Coat Tech.* 2020. <https://doi.org/10.1016/j.surfcoat.2020.126607>.
25. Danielewski H, Antoszewski B. Properties of laser additive deposited metallic powder of Inconel 625. *Open Eng.* 2020;10:484–90. <https://doi.org/10.1515/eng-2020-0046>.
26. Borgh I, Hedström P, Blomqvist A, Ågren J, Odqvist J. Synthesis and phase separation of (Ti, Zr)C. *Acta Mater.* 2014. <https://doi.org/10.1016/j.actamat.2013.11.074>.
27. Ma T, Hedström P, Odqvist J. Effect of synthesis temperature and aging on the microstructure and hardness of Ti-Zr-C. *Int J Refract Met H.* 2018. <https://doi.org/10.1016/j.jrmhm.2018.02.001>.
28. <https://imagej.en.softonic.com/download>
29. Graboś A, Rutkowski P, Huebner J, Kozień D, Zhang Sh, Kuo Y-L, Kata D, Hayashi Sh. Oxidation performance of spark plasma sintered Inconel 625-NbC metal matrix composites. *Corros Sci.* 2022. <https://doi.org/10.1016/j.corsci.2022.110453>.
30. Kong D, Dong C, Ni X, Zhang L, Man C, Zhu G, Yao J, Yao J, Wang L, Cheng X, Li X. Effect of TiC content on the mechanical and corrosion properties of Inconel 718 alloy fabricated by a high-throughput dual-feed laser metal deposition system. *J Alloy Compd.* 2019. <https://doi.org/10.1016/j.jallcom.2019.06.317>.
31. Poloczek T, Lont A, Górka J. The structure and properties of laser-clad Inconel 625/TiC composite coatings. *Materials.* 2023. <https://doi.org/10.3390/ma16031265>.
32. Huebner J, Kata D, Kusiński J, Rutkowski P, Lis J. Microstructure of laser clad carbide reinforced Inconel 625 alloy for turbine blade application. *Ceram Int.* 2017. <https://doi.org/10.1016/j.ceramint.2017.03.194>.
33. Long F, Yoo YS, Jo CY, Seo SM, Jeong HW, Song YS, Jin T, Hu ZQ. Phase transformation of  $\eta$  and  $\sigma$  phases in an experimental nickel-based superalloy. *J Alloy Compd.* 2009. <https://doi.org/10.1016/j.jallcom.2008.11.121>.
34. El-Bagoury N, Mohsen Q. Gamma prime and TCP phases and mechanical properties of thermally exposed nickel-base superalloy. *Phase Transit.* 2011. <https://doi.org/10.1080/01411594.2011.582379>.
35. Badiger RI, Narendranath S, Srinath MS. Microstructure and mechanical properties of Inconel-625 welded joint developed through microwave hybrid heating. *P I Mech Eng B-J Eng.* 2017. <https://doi.org/10.1177/0954405417697350>.
36. Graboś A, Rutkowski P, Huebner J, Nieroda P, Kata D, Hayashi S. Thermal properties of Inconel 625-NbC metal matrix composites (MMC). *Mater Des.* 2022. <https://doi.org/10.1016/j.matdes.2022.111399>.
37. Gasparrini C, Chater R, Horlait D, Vanseperre L, Lee WE. Zirconium carbide oxidation: kinetics and oxygen diffusion through

- the intermediate layer. *J Am Ceram Soc.* 2018. <https://doi.org/10.1111/jace.15479>.
38. Roma Rao GA, Venugopal V. Kinetics and mechanism of the oxidation of ZrC. *J Alloy Compd.* 1994. [https://doi.org/10.1016/0925-8388\(94\)90042-6](https://doi.org/10.1016/0925-8388(94)90042-6).
  39. Ge T, Chen L, Gu P, Ren X, Chen X. Microstructure and corrosion resistance of TiC/Inconel 625 composite coatings by extreme high speed laser cladding. *Opt Laser Technol.* 2022. <https://doi.org/10.1016/j.optlastec.2022.107919>.
  40. Zhou H, Chen Y, Sui Y, Lv Y, Zhu Z, Yang L, He Z, Li C, Fang K. Effect of iron ion on corrosion behavior of Inconel 625 in high-temperature water. *Hindawi Scanning.* 2020. <https://doi.org/10.1155/2020/9130362>.
  41. Colas J, Charpentier L, Balat-Pichelin M. Oxidation in air at 1400 K and optical properties of Inconel 625, FeCrAlloy and kanthal super ER. *Oxid Met.* 2020. <https://doi.org/10.1007/s11085-020-09959-6>.
  42. Feng J, Yuan G, Mao L, Leão JB, Bedell R, Ramic K, Stefanis E, Zhao Y, Vidal J, Liu L. Probing layered structure of Inconel 625 coatings prepared by magnetron sputtering. *Surf Coat Technol.* 2020. <https://doi.org/10.1016/j.surfcoat.2020.126545>.
  43. Staszewska K, Scendo M. Mechanism and kinetics oxidation of Inconel 617 and 625 alloys. *Technical Issues.* 2016;1:82–9.
  44. Biedunkiewicz A, Gordon N, Straszko J, Tamir S. Kinetics and thermal oxidation of titanium carbide and its carbon nano-composite in dry air atmosphere. *J Therm Anal Calorim.* 2007. <https://doi.org/10.1007/s10973-006-8222-x>.
  45. Lavrenko VA, Glebov LA, Pomitkin AP, Chuprina VG, Protsenko TG. High-temperature oxidation of titanium carbide in oxygen. *Oxid Metal.* 1975. <https://doi.org/10.1007/BF00613231>.
  46. Niemeyer D. The gas sensitive material  $\text{Cr}_{(2-x)}\text{Ti}_{(x)}\text{O}_3$ . PhD, 2001, ProQuest LLC. 2016. [https://www.researchgate.net/publication/342329347\\_The\\_gas\\_sensitive\\_material\\_Cr\\_2-x\\_Ti\\_x\\_O3](https://www.researchgate.net/publication/342329347_The_gas_sensitive_material_Cr_2-x_Ti_x_O3). Accessed 2016
  47. Hardcastle FD, Wachs IE. Determination of niobium-oxygen bond distances and bond orders by Raman spectroscopy. *Solid State Ionics.* 1991. [https://doi.org/10.1016/0167-2738\(91\)90153-3](https://doi.org/10.1016/0167-2738(91)90153-3).
  48. Ding S, Zhao J, Yu Q. Effect of zirconia polymorph on vapor-phase ketonization of propionic acid. *Catalysts.* 2019. <https://doi.org/10.3390/catal9090768>.
  49. Bauer AJR. ZrO<sub>2</sub> phase identification with Raman spectroscopy. [https://tsi.com/getmedia/6485a12e-d8bb-4f1a-a74e-3b89738705d6/Identification\\_of\\_ZrO2\\_Phase\\_w\\_Raman\\_Spectroscopy\\_App\\_Note\\_RAMAN-020\\_A4-web?ext=.pdf](https://tsi.com/getmedia/6485a12e-d8bb-4f1a-a74e-3b89738705d6/Identification_of_ZrO2_Phase_w_Raman_Spectroscopy_App_Note_RAMAN-020_A4-web?ext=.pdf)
  50. Kim YK, Jang HM. Lattice contraction and cation ordering of ZrTiO<sub>4</sub> in the normal-to-incommensurate phase transition. *J Appl Phys.* 2001. <https://doi.org/10.1063/1.1368871>.
  51. McConnell AA, Anderson JS, Rao CNR. Raman spectra of niobium oxides. *Spectrochim Acta.* 1976. [https://doi.org/10.1016/0584-8539\(76\)80291-7](https://doi.org/10.1016/0584-8539(76)80291-7).
  52. Bai Y, Qu S, Jia Y, Zhang L, Zhu G, Feng A, Wu G, Wu H. Cr<sub>2</sub>O<sub>3</sub> nanocrystal anode materials with improved cyclic stability for lithium ion batteries. *J Mater Sci-Mater El.* 2018. <https://doi.org/10.1007/s10854-018-9279-6>.
  53. Martiz A, Károly Z, Trif L, Mohai M, Bereczki L, Németh P, Molnár Z, Menyhárd A, Pawar RP, Tekale S, Kótai L. Plasma-assisted preparation of nano-(ZrC, ZrO<sub>2</sub>)/carbon composites from Zr-loaded sulfonated styrene-divinylbenzene copolymers. *J Therm Anal Calorim.* 2022. <https://doi.org/10.1007/s10973-022-11236-4>.
  54. Martiz A, Károly Z, Domján A, Mohai M, Bereczki L, Trif L, Farkas A, László K, Menyhárd A, Kótai L. Nano-ZrO<sub>2</sub>@C, Nano-(ZrC, ZrO<sub>2</sub>)/C and Nano-ZrC/C composites prepared by plasma-assisted carbonization of Zr-loaded iminodiacetate-functionalized styrene-divinylbenzene copolymers. *Inorganics.* 2022. <https://doi.org/10.3390/inorganics10060077>.

**Publisher's Note** Springer Nature remains neutral with regard to jurisdictional claims in published maps and institutional affiliations.